Original Article

On the microstructural evolution and failure mechanism in laser powder bed fusioned Ti−6Al−4V during low cycle fatigue at room and elevated temperatures

Alok Gupta [a,b,*], Chris J. Bennett [b], Wei Sun [b], Nigel Neate [c]

[a] ITP Aero UK Ltd, Harrier Business Park, Dorey Way, Hucknall, NG15 6EU, United Kingdom

[b] Gas Turbine and Transmissions Research Centre (G2TRC), Faculty of Engineering, University of Nottingham, University Park, Nottingham, NG7 2RD, United Kingdom

[c] Nanoscale and Microscale Research, University of Nottingham, University Park, Nottingham, NG7 2RD, United Kingdom

ARTICLE INFO

ABSTRACT

Microstructural features and their evolution during cyclic deformation directly impact the low cycle fatigue (LCF) life of additively manufactured Laser Powder Bed Fusion (LPBF) Ti−6Al−4V. Tensile and strain controlled LCF tests were performed at room (RT) and elevated temperature (ET, @ 400 °C) to study the cyclic softening behaviour and failure mechanism of LPBF Ti−6Al−4V. The evolution of α' grains and free dislocation density were studied using Electron Backscatter Diffraction (EBSD). LPBF Ti−6Al−4V has greater tensile strength than conventionally manufactured wrought Ti−6Al−4V due to its microstructure, with fine α' needles which provide small slip lengths. For cyclic loading at ET, the interaction between the dislocations increases which in-turn increases the ability of material to overcome the obstacles to dislocation motion, resulting in higher cyclic softening compared to the RT test. During cyclic deformation, evolution of dislocation substructures takes place to subsequently produce Low Angle Boundaries (LABs) inside the prior α' grains. The LABs progressively lead to nucleation and coalescence of voids with fatigue cycles, eventually leading to fracture. An increase in strain range (i.e. plasticity level) causes more significant dislocation pile-up, contributing to a greater amount of cyclic softening. The lack of fusion voids or pores, present at or near the surface, and microcracks, present at the rough surface, act as the crack initiation locations which propagate to cause fracture of the LPBF material under LCF loading, where the primary mode of fatigue fracture observed is intergranular.

© 2022 The Authors. Published by Elsevier B.V. This is an open access article under the CC BY license (http://creativecommons.org/licenses/by/4.0/).

---

* Corresponding author.
  E-mail address: alok.gupta@nottingham.ac.uk (A. Gupta).

1.   Introduction

In the Laser Powder Bed Fusion (LPBF) Additive Manufacturing (AM) process, a high energy laser beam travels over the build area in a carefully controlled speed and scan pattern to selectively melt the powder layer spread over the build plate, as per the designed parameters [1—3]. The LPBF process is used to build small to medium quantities of complex net shape components with moderate to high surface finish [4]. The titanium alloy Ti—6Al—4V is frequently used to fabricate components in the biomedical and aerospace industries due to its superior strength to weight ratio, good corrosion resistance and moderate service temperature capability [5]; however, the main challenge when using Ti—6Al—4V in high temperature applications is that environmental degradation such as high temperature oxidation, alpha case formation etc. could occur [6]. Ti—6Al—4V is a dual-phase alloy at room temperature and benefits from the combination of the strength of the α phase and the ductility of the β phase [7]. Although LPBF processed Ti—6Al—4V offers good mechanical strength compared to conventionally produced Ti—6Al—4V, its fatigue strength is observed to be much lower and produces a higher scatter in fatigue data [5]. Lack of fusion, shrinkage or entrapped gases during melting and solidification produce defects which are unavoidable in the LPBF process and are understood to have a significant effect on the fatigue strength of LPBF Ti—6Al—4V [1,5,8].

The repeated heating and rapid cooling of molten metal in the LPBF process results in a complex microstructure of LPBF Ti—6Al—4V. Upon cooling from the melting temperature (1670 °C), the melt starts to solidify into the β phase and β grains (of bcc structure) start to form. When the temperature drops below the β transus temperature (995 °C), the β phase transforms into the α' martensitic phase at high cooling rates (>410 °C/s) and to the α phase at slow cooling rates (<20 °C/s) [9]. In the LPBF process, the cooling rate is fast, therefore the nucleation of α' phase (needle shape with high aspect ratio) occurs both within and at the boundaries of the prior β grains simultaneously, through diffusion-less/displacive transformation [10,11]. The α' needles grow from these locations and meet each other to form a basketweave type of microstructure which comes with high free dislocation density and/ or twins [10].

Poor surface roughness, residual stresses and characteristic microstructure are other influencing parameters which affect the fatigue performance of LPBF Ti—6Al—4V and causes anisotropy in its fatigue response [12]. Furthermore, the high affinity of Ti—6Al—4V to oxygen causes the formation of a very thin oxygen layer (OL) on the surface of the alloy even in air at Room Temperature (RT) [6] which again has deleterious effects on the fatigue life of Ti—6Al—4V. A good understanding of the fatigue behaviour of LPBF Ti—6Al—4V is, therefore, a prerequisite to successfully deploying this material in safety critical applications [5]. To date, several research studies have been performed to develop the understanding of fatigue (both low and high cycle fatigue) response of LPBF Ti—6Al—4V; however, the low cycle fatigue (LCF) performance, where plasticity and elastic—plastic fracture mechanics play a key role, is relatively unexplored for LPBF Ti—6Al—4V. Classical strain-controlled tests are often performed to investigate the

cyclic performance of metallic materials under moderate to large plastic strains for a low number of cycles, both at RT and at elevated temperatures (ET). The softening behaviour observed in the low cyclic response at RT and ET typically involves combined visco-plasticity and creep-fatigue interactions. Several mechanisms such as: (i) changes in microstructure, (ii) slip bands and (iii) the presence of pores and voids are responsible for softening in each of these stages [13,14]. Furthermore, the mechanisms related to microstructural changes that are responsible for cyclic softening are: (i) annihilation of dislocations introduced during martensitic transformation, (ii) changes from the original lath structure to equiaxed sub-grains, and (iii) coarsening of precipitates [15—18].

The cyclic deformation and softening response of an $\alpha+\beta$ titanium alloy is strain amplitude dependent [14,15]. According to Huang et al. [16], the primary α phase (α_p), transformed β phase and embedded fine precipitated secondary α phase in the β matrix (α_s) play critical roles in the softening behaviour of the alloy at different strain levels and at different cycling stages. Luquiau et al. [15] revealed that the cyclic softening is due to a decrease in both the isotropic and kinematic components of the stresses. The decrease in the kinematic component of stresses (internal softening) is associated with a process of homogenisation of α_p particles, which happens due to yielding through the microstructure, whereas the isotropic softening or the effective stress softening is due to annihilation of dislocations enhanced by cross slip in the α-phase [15]. The cyclic softening behaviour is microstructure dependent in Ti—6Al—4V [17,18]. Prasad et al. [17] found that the cyclic softening behaviour in Ti—6Al—4V is due to the rearrangement of dislocations and concluded that the strain accumulation needed to nucleate a crack in the α phase is generally lower than that in the β phase which causes primary α grains (α_p) with large grain boundaries to become the weaker sites for internal crack initiation. According to Han et al. [18], the equiaxed microstructure exhibited the most significant cyclic softening behaviour, whilst the Widmanstätten microstructure exhibited the lowest, and the softening behaviour was due to the plasticity of the primary α phase [18]. Prasad et al. [17] also defined a strength parameter STR (Ultimate Tensile Strength/Yield Strength). If the value of STR is less than 1.2, then this indicates that some level of cyclic softening is highly likely.

Bressan et al. [13] carried out a study to understand the effect of heat treatment, build orientation and the presence of voids on the cyclic plastic behaviour of Ti—6Al—4V built using the LPBF process. They found that although the build orientation did not influence the size of the grains or void morphology or density, the effect of build orientation on the cyclic softening and hardening behaviours was noticeable [13]. Also, the heat treatment increased material hardening without significantly affecting its elastic-plastic cyclic behaviour, but led to early failure. Whereas, under the initial applied cyclic stress, micro-cracks were initiated from the voids and pores present, directly impacting the material softening behaviour [13]. Ren et al. [14] carried out fully reversed strain controlled LCF tests at room temperature at

Table 1 – Process parameters used to build LPBF tensile and LCF specimens in Ti–6Al–4V.

Parameter	Value
Laser Power	170 W
Laser Scan Speed	1250 mm/s
Hatch Width	5 mm
Hatch Distance	0.1 mm
Hatch overlap	0 mm
Table displacement [22]	30 μm

different strain amplitudes to study the low cycle fatigue properties of Laser Solid Formed (LSF) Ti–6Al–4V and suggested that the cyclic softening was strongly dependent on the strain amplitude, increasing with increasing strain amplitude. They also suggested a microstructure-based multistage fatigue (MSF) model, which seemed to predict the LCF life for LSF Ti–6Al–4V with reasonably good agreement against the experimental data [14]. Also, the high affinity of Ti–6Al–4V to oxygen at elevated temperature (above 400 °C) causes the formation of a very thin oxygen layer and an oxygen diffusion zone develops, which significantly deteriorates the tensile and fatigue performance of Ti–6Al–4V [19,20]. For this reason, the maximum service temperature for Ti–6Al–4V in aerospace applications is often limited to less than 400 °C [19,20].

In the present study, the LCF behaviour of LPBF Ti–6Al–4V at different Strain Ranges (SRs) was studied through strain-controlled tests, both at RT (20 °C) and at ET (400 °C). The study explores the role of microstructure with an aim to identify the prominent mechanisms behind the cyclic softening behaviour in LPBF Ti–6Al–4V. Furthermore, the microstructure evolution was studied by examining the change from the baseline material, in terms of the grain structure and Kernel Average Misorientation (KAM) (representing free dislocation density) in the samples from interrupted tests at ET, using the Electron Backscatter Diffraction (EBSD) technique. Additionally, the fracture surfaces of the failed specimens were characterised and the relationship between the fracture mechanism and role of defects on the LCF behaviour of LPBF Ti–6Al–4V was explored. The characterisation included the tensile and cyclic stress responses, fatigue life, fracture surface, X-ray CT scan of intermediate stages of the cyclic tests followed by a microstructural investigation of the initial, intermediate (through interrupted tests) and failed stages for fatigue tests at elevated temperatures.

2. Material and experimental programme

2.1. Ti–6Al–4V *powder and build parameters*

Ti–6Al–4V (Grade 23) Extra Low Interstitials (ELI) plasma atomised powder (Supplied by LPW Technology, UK), with a measured chemical composition of Al 6.4, V 4.0, Fe 0.19, O 0.12, N 0.02, H 0.002, C 0.02, Ti Bal (wt. %), in line with ASTMB348 [21], was used in this study. From the data analysis carried out by the supplier, the powder size was distributed between 15 and 45 μm with a mean of 30 μm. This distribution analysis also found that only 3% of powder particles were below 16 μm in size and only 2% of the powder particles were above 45 μm in size.

The tensile and LCF test specimens were built using the commercially available EOS M280 a.m. machine. The EOS machine has a chamber size of 250 mm × 250 mm x 325 mm, operates in argon atmosphere and has a substrate of Grade 5 Ti–6Al–4V preheated to 35 °C. The build parameters are given in Table 1 below:

Post build, the test specimens were cut from the substrate using wire-EDM. Subsequently, the build supports were removed and aqua blasting was performed to remove loosely sintered powder and improve surface finish. After this, a stress relief was carried out at 650 °C for 3 h in an argon atmosphere, followed by furnace cooling to RT.

2.2. *Build layout, specimen geometry and test matrix*

2.2.1. *Tensile test specimen and test equipment*
As part of this study, the tensile strength of LPBF Ti–6Al–4V was characterised for tests at RT and ET. The tensile specimens were built in the vertical direction, i.e. were aligned to the Z direction (designated as the Z orientation [23,24]), and the key dimensions of the specimens are shown in Fig. 1. The threads at the two grip ends were machined, but the central gauge sections of the specimens were left as-built. The test parameters for the two tensile tests are listed in Table 2.

Tensile tests were performed using an electric Mayes 250 test rig which was fitted with a Mayes 250 kN load cell. A SF2170B three zone split resistance furnace, with rated voltage of 230 V and power of 1000 W, was used to maintain the test temperature in the furnace. Three K-type thermocouples, spaced along the gauge length, were used to measure the surface temperature of the specimens. A pair of LVDTs were used to measure the gauge extension. The load application
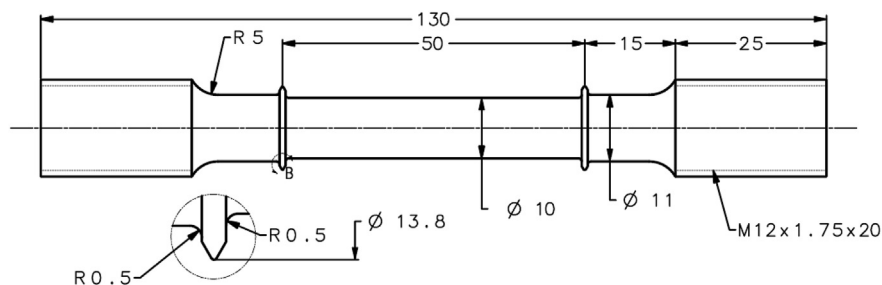
Fig. 1 – Dimensions of tensile specimen (mm)

Table 2 − Tensile test matrix.

Test Identification Number (#)	Build Orientation - Surface Condition	Temperature (°C)	Strain Rate (s^{-1})
T-RT	Vertical as-built	20	0.0002
T-ET	Vertical as-built	400	0.0002

was parallel to the build direction, i.e. was perpendicular to the layer deposition direction.

2.2.2. LCF test specimens and test equipment

Since the loading of components in an application can be complex, in this study, cyclic tests were performed to try to accurately establish the material fatigue behaviour and SR dependent cyclic plasticity. For the LCF tests, the 5 mm diameter solid cylindrical fatigue specimens, with a gauge length of 10 mm, as shown in Fig. 2, were built to the ISO 12106 standard [25].

Fully reversed strain controlled LCF tests (at displacement ratio of R = −1) at RT and ET with a strain rate of 0.002 s^{-1} were carried out using the saw-tooth type (SWT) waveform shown in Fig. 2(b) and data was acquired continuously until specimen fracture to investigate the cycles to failure and softening/hardening of LPBF Ti−6Al−4V under LCF loading. The LCF tests were performed at predefined SRs in the range of $\pm 0.8\% \leq SR \leq \pm 1.5\%$, and the LCF test matrix is presented in Table 3. The selected temperatures for the LCF tests enveloped the operating temperatures in the intended application, i.e. for aero-engine externals parts. Furthermore, two interrupted cyclic tests were also carried out at a SR of $\pm 1.2\%$ and at ET to investigate the microstructural evolution during the progression of cyclic loading. The interrupted tests were planned to be stopped once an intended number of cycles was reached.

The LCF tests were conducted in air on a Tinius Olsen H25KS electromechanical testing system fitted with a Tinius Olsen DSCCTOL 25 kN pancake style load cell and a Severn

Thermal Solutions SF2107 split section resistance furnace. The temperature along the gauge length of the specimen was controlled using three K-type thermocouples spaced out along the specimen surface. The strain values were measured using a high temperature side-contact extensometer.

2.3. Microstructure characterisation

For metallographic characterisation, the sample sections were cut and hot mounted in bakelite resin. The mounted samples were polished first with SiC papers (p240, 400, 800 and 1200 grit sizes), followed by a fine polish using a plane-cloth (6 μm) and alpha-cloth (1 μm) in diamond suspension, and finally using the chemi-cloth in colloidal silica solution. Only the samples for Scanning Electron Microscope (SEM) examination were etched using Keller's reagent (190 ml of distilled water, 5 ml of nitric acid, 3 ml of hydrochloric acid and 2 ml of hydrofluoric acid) with 20 s immersion. A Nikon Eclipse LV100ND microscope was used to carry out optical microscopy for preliminary examination of the microstructure. SEM examinations were carried out using a Quanta FE600 scanning electron microscope for microstructural characterisation. Additionally, a JEOL 7100F Field Emission Gun Scanning Electron Microscope (FEG-SEM) was used to perform EBSD scans for detailed microstructure characterisation. The FEG-SEM was equipped with an Oxford Instruments AZtec HKL Advanced EBSD system (with NordlysMax3) for crystallographic characterisation. The EBSD scans were conducted at 15 kV with a step size of 0.25 μm and the scan area chosen was 150 μm × 150 μm. The postprocessing software HKL channel and AZtec Crystal software were used to analyse the EBSD data. The grains were identified based on a 10° mis-orientation criteria, i.e. the continuous presence of a boundary of more than 10° was used to distinguish the grains. The AZtec Crystal software was used to produce Kernel Average Misorientation (KAM) plots from the EBSD results. The KAM plots were build using a square Kernel shape in 3 × 3 size, with a maximum angle of 7°.
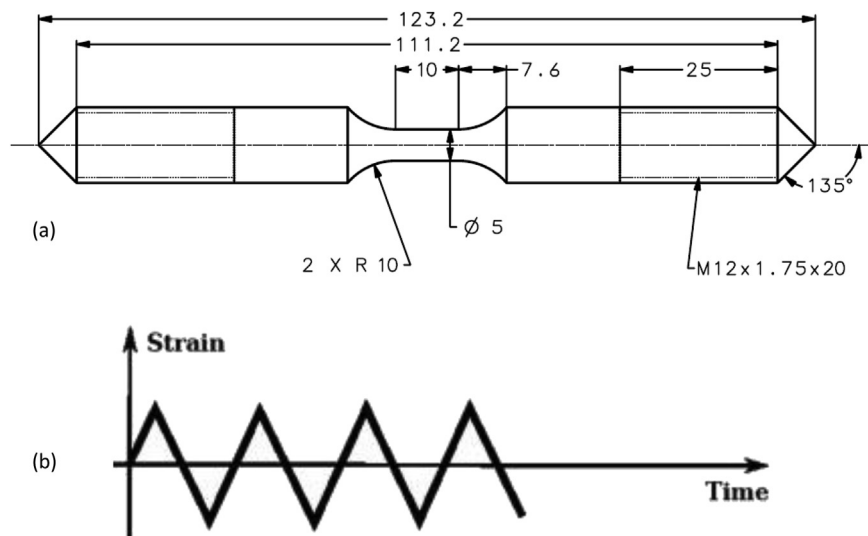
Fig. 2 − LCF tests: (a) dimensions of LCF specimen (mm), and (b) saw-tooth type waveform used for LCF tests

Table 3 – Cyclic strain-controlled test matrix.				
Test No.	Test Identification Number (#)	Description	Temperature°C	Strain Range (SR) (%)
1	L-RT1	Test to fracture	20	±0.8
2	L-RT2	Test to fracture	20	±1.2
3	L-RT3	Test to fracture	20	±1.5
4	L-ET1	Test to fracture	400	±0.8
5	L-ET2	Test to fracture	400	±1.2
6	L-ET3	Test to fracture	400	±1.5
7	L-ET4	First interrupted test	400	±1.2
8	L-ET5	Second interrupted test	400	±1.2

2.4. Defect characterisation

To study the morphology and distribution density of defects, X-ray CT (3D computed tomography) scans were carried out on vertical and horizontal as-built representative samples using a Nikon XTH225 Reflection Target X-ray machine. The X-ray CT scan parameters are listed in Table 4.

2.5. Hardness characterisation

Microhardness (Vickers scale) tests were carried out using a Wilson VH3100 automatic hardness testing machine using a load of 500 gf with a grid spacing of 50 μm × 50 μm. Hardness tests were performed on the tested LCF specimens on a longitudinal cut face containing the build/loading axis to study the material hardness in the necked region.

3. Results

3.1. Mechanical responses

3.1.1. Tensile properties
The engineering stress-strain curves from the tensile tests performed at RT and ET are presented in Fig. 3 and the basic mechanical properties are summarised in Table 5, where it can be seen that the Yield Strength (PS, (0.2% Proof Strength) and Ultimate Tensile Strength (UTS)) were significantly lower, but the material ductility was higher for the ET test compared to the RT test. The strength values for the LPBF material are also compared with those of the annealed Ti–6Al–4V bar, where it can be seen that the PS and UTS values for LPBF Ti–6Al–4V are higher than those of the annealed Ti–6Al–4V bar.

At ET, the resistance to plastic flow i.e. material strength reduces due to the enhanced migration and annihilation of dislocations, which causes the material to become more ductile as observed in Fig. 3 [26,27].

Table 4 – X-ray CT scan parameters.	
CT Parameter	Vertically Built Sample
X-ray voltage (kV)	220
Current (μA)	200
Exposure time (s)	0.7
Voxel resolution (μm)	11
Number of projections	3141

Table 5 also presents the values of strength ratio STR from the two tensile results performed. As shown in Table 5, for both the tests performed, the STR is less than 1.2, suggesting that some level of cyclic softening can be expected during the cyclic performance of LPBF Ti–6Al–4V [17].

3.1.2. Low cycle fatigue behaviour
In order to illustrate the influence of temperature and SR on the cyclic response of the LPBF Ti–6Al–4V, the evolution of the hysteresis loops are discussed in the following subsections for the tests carried out at both RT and ET. The hysteresis loops are plotted for the chosen discrete fatigue cycles such that the hysteresis loops are spaced out uniformly from the start to the end of the test, which allows a gradual evolution of the shape of hysteresis loops, clearly showing a drop in stress to be observed. The LCF fatigue test results are summarised in Table 6, where it can be seen that the number of cycles to failure decreases with increasing test SR for both RT and ET LCF tests.

3.1.2.1. Tests at RT. The cyclic performance of LPBF Ti–6Al–4V at RT is shown in Fig. 4(a)–4(c) with increasing SR, respectively. The stress − strain hysteresis loops shown in Fig. 4(a)–4(c) suggest a drop in stress range with increasing number of cycles, i.e. cyclic softening. Also, as we move from
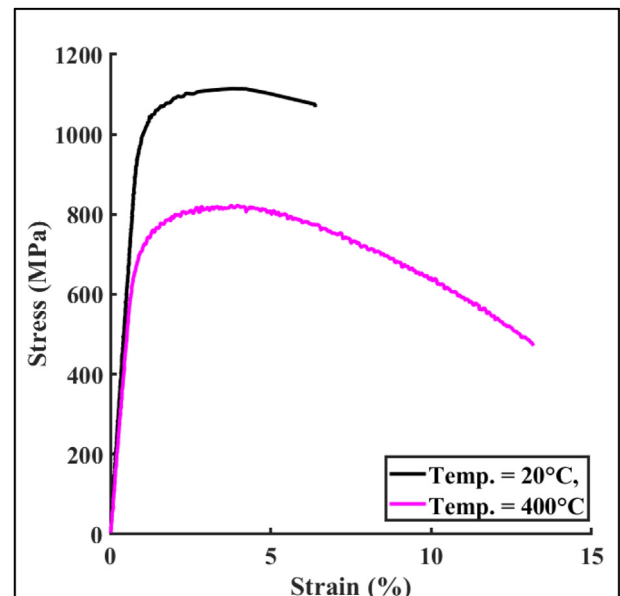
Fig. 3 – Tensile testing-engineering stress-strain curves

Table 5 — Tensile test data.

Test Identification Number (#)	Temperature (°C)	Young's Modulus	PS (σ_y, MPa)	UTS (σ_u, MPa)	Ductility (%)	STR
T-RT	20	116,000	1020	1114	6.4	1.09
T-ET	400	95,727	696	827	13.2	1.19
Annealed Ti—6Al—4V Bar [28]	20	—	861	930	10	1.08

Fig. 4(a)—4(c), the hysteresis loops appear to have become increasingly wider due to increase in SR/test plasticity level.

Variations in the maximum (σ_{max}), minimum (σ_{min}) and mean (σ_{mean}) stresses vs cycle number are shown in Fig. 4(d)-4(f). In Fig. 4(d)-4(f), cyclic softening can be seen for each test, and the typical shape of the curves shows the typical three stages previously described. A noticeable difference in the maximum stress in Stage 1 was observed between the L-RT1 and L-RT2 tests, see Fig. 4(d) and (e), respectively. However, the difference in the maximum stress in Stage 1 was much smaller between the L-RT2 and L-RT3 tests, see Fig. 4(e) and (f), respectively. Also, from Fig. 4(d)-4(f), a slight asymmetry was observed in the cyclic softening response in the σ_{max} and σ_{min} parts for each of the RT cyclic tests.

3.1.2.2. *Tests at ET*. The performance from the ET cyclic tests at three different SRs are shown in Fig. 5. On comparing the softening relationships in Figs. 4 and 5, the rate of softening is found to be greater for the ET tests than the RT tests for the corresponding SR. The hysteresis loops are increasingly wider with increasing SR, i.e. increase in test plastic strain. Also, the hysteresis loops for the ET tests are wider than the hysteresis loops for the RT test for each SR, which is due a reduction in stiffness at ET where a lower PS is compensated by an increase in the level of plasticity. Furthermore, from Fig. 5a and b and, at a high number of test cycles, the width of hysteresis loops is bigger in the tension portion of the hysteresis loop than in compression, which is clearly evident for L-ET1 and L-ET2 tests; however, this difference in shape of the tension and compression part of the hysteresis loops is small for L-ET3 test, which perhaps is due to the failure of the L-ET3 test specimen at a lower number of cycles as seen in Fig. 5(c).

The performance of the σ_{max}, σ_{min} and σ_{mean} stresses for the ET cyclic tests are shown in Fig. 5(d)-5(f). The maximum stress in Stage 1 is higher for L-ET2 tests when compared to the L-ET1 test, whereas the difference in maximum stress in Stage 1 is insignificant for the F-ET2 and F-ET3 tests. It is also observed that most Stage 1 softening happens within the first

few cycles (~20 cycles) before arriving at the quasi-saturated state of softening in Stage 2.

From Fig. 5(d)—5(f), the shape of maximum and minimum stress curves shows an asymmetric response and indicates that the amount cyclic softening is higher in tension than in compression for LCF tests at ET. This asymmetric response in tension and compression also affects the mean stress response. The asymmetry of the hysteresis loops at ET is believed to be due to the asymmetric material response of LPBF Ti—6Al—4V in terms of the PS and Young's modulus in the tensile and compressive loading [17].

3.2. Cyclic softening and mechanical energy variations

Wrought Ti—6Al—4V has been shown to have superior LCF life than that of LPBF Ti—6Al—4V due to its fine equiaxed α grains, while the reduced ductility, surface roughness and intrinsic defects are linked to the lower LCF life of LPBF material [14]. To characterise the LCF behaviour of LPBF Ti—6Al—4V, the softening behaviour at different SRs is plotted in Fig. 6(a) and Fig. 6(b) for the RT and ET tests, respectively. From Fig. 6, the LPBF Ti—6Al—4V exhibits a lower starting stress amplitude for ET tests than the RT tests. Also, an accelerated and larger amount softening in Stage 3 can be seen for ET tests, which is due to damage localisation, an increase in ductility levels and an increase in test plastic strains.

3.3. Physical characterisation

3.3.1. *Microstructure of as received LPBF Ti—6Al—4V*
The optical micrograph of the vertical cut section (along the build direction) is shown in Fig. 7. The microstructure is characterised by the prior β grain boundaries with its epitaxial growth running across multiple layers. The average width of prior columnar β grains is between 80 and 100 μm. The SEM micrograph of the section along the build direction in Fig. 8(a) shows the acicular martensitic α′ phase (needle shape). In the section transverse to the build direction, the α′

Table 6 — Cyclic strain-controlled test results and resulting cycles to failure.

| Test No.	Test Identification Number (#)	Temperature °C	Strain Range (SR) (%)	Number of Cycles to Failure	Comment
1	L-RT1	20	±0.8	1899	Fractured
2	L-RT2	20	±1.2	294	Fractured
3	L-RT3	20	±1.5	59	Fractured
4	L-ET1	400	±0.8	965	Fractured
5	L-ET2	400	±1.2	319	Fractured
6	L-ET3	400	±1.5	144	Fractured
7	L-ET4	400	±1.2		First interrupted test, interrupted at 160 cycles, Unfractured
8	L-ET5	400	±1.2	189	Second interrupted (planned) test, Specimen fractured prematurely
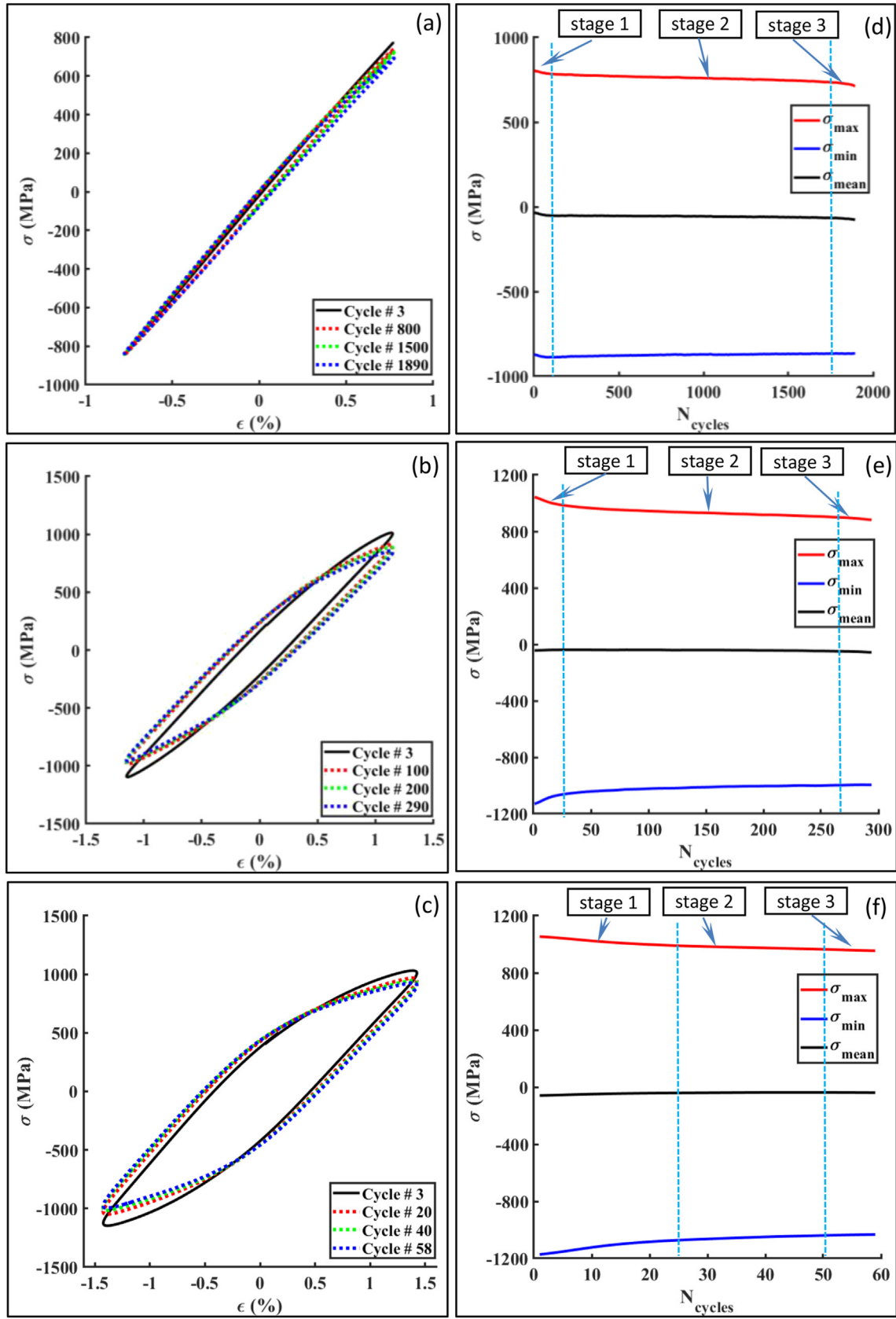
Fig. 4 − Low cycle fatigue tests at RT: (a) discrete hysteresis loops at SR = ±0.8% (L-RT1), (b) discrete hysteresis loops at SR = ±1.2% (L-RT2), (c) discrete hysteresis loops at SR = ±1.5% (L-RT3), (d) cyclic softening behaviour at SR = ±0.8% (L-RT1), (e) cyclic softening behaviour at SR = ±1.2% (L-RT2), and (f) cyclic softening behaviour at SR = ±1.5% (L-RT3), where RT: Room temperature, SR: Strain range
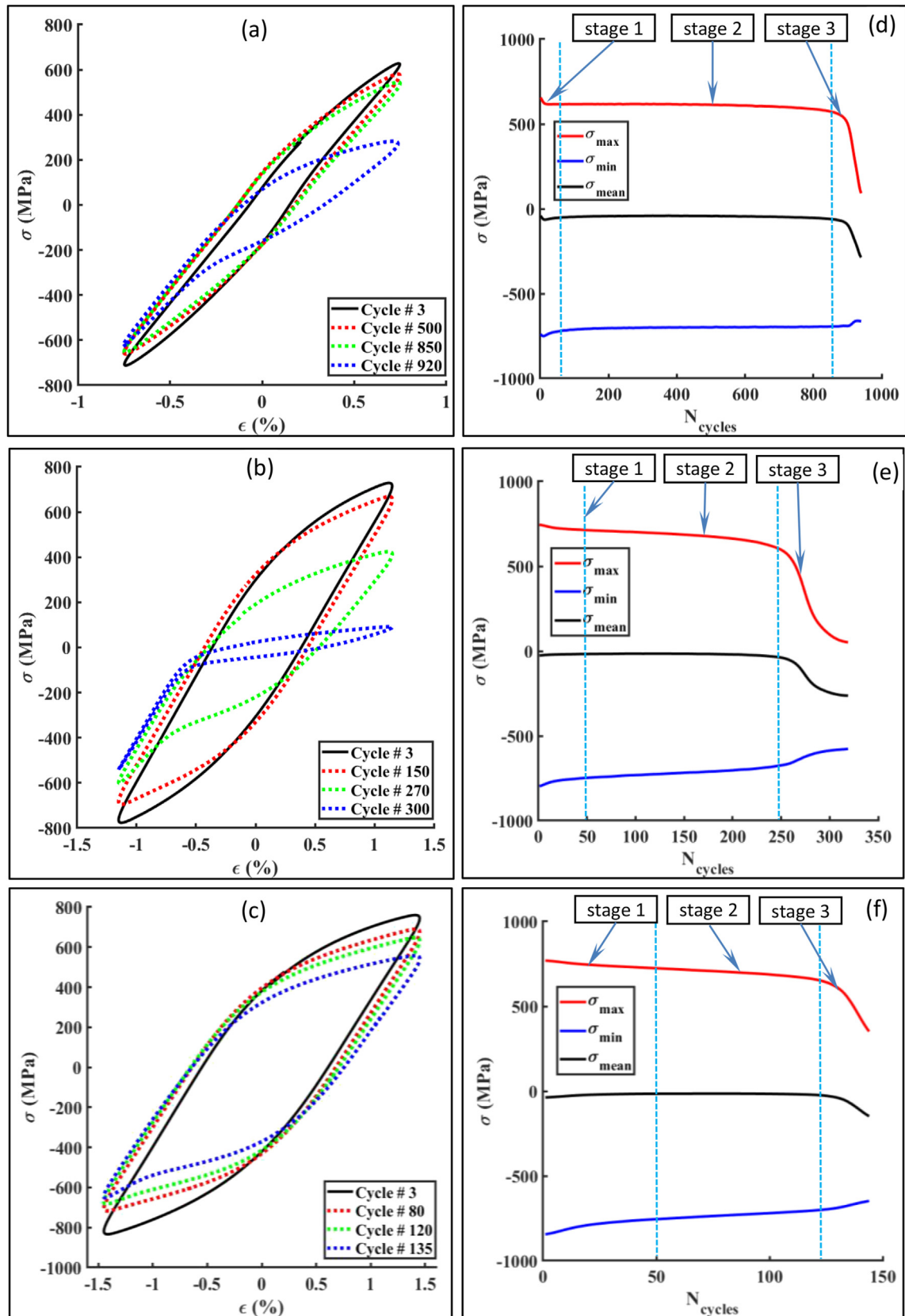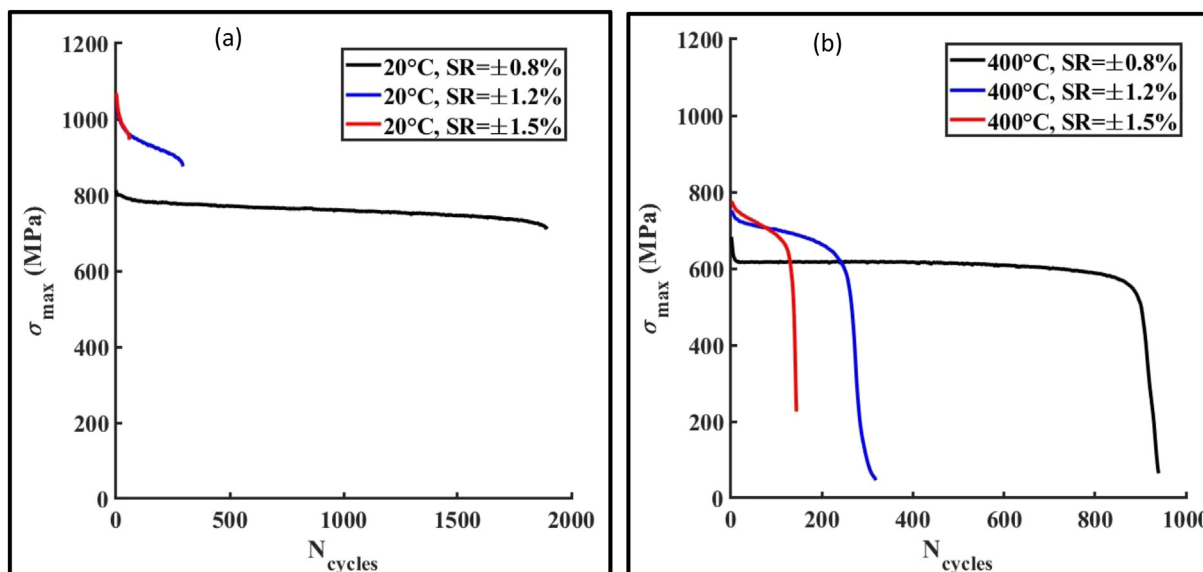
Fig. 5 − Low cycle fatigue tests at ET: (a) discrete hysteresis loops at SR =±0.8% (L-ET1), (b) discrete hysteresis loops at SR = ±1.2% (L-ET2), (c) discrete hysteresis loops at SR = ±1.5% (L-ET3), (d) cyclic softening at SR = ±0.8% (L-ET1), (e) cyclic softening behaviour at SR = ±1.2% (L-ET1), and (f) cyclic softening behaviour at SR = ±1.5% (L-ET1), where ET: Elevated temperature, SR: Strain range

Fig. 6 — Cyclic softening behaviour of LPBF Ti—6Al—4V material, max stress evolution at different SR: (a) Tests at RT (20°), and (b) Tests at ET (400 °C), where RT: Room temperature, ET: Elevated temperature, and SR: Strain range

needles appear to span within the prior β grain boundaries as seen in Fig. 8(b) [10].

3.3.2. Fractographic features

3.3.2.1. Tensile fractured specimens. The T-RT and T-ET tensile specimens both exhibited a typical cup and cone type failure with their central portion being almost flat, as shown in the SEM images in Fig. 9. The fractured surface appears to be rough with shear lips observed in both the fractured specimens (Fig. 9(a) and (e)). With a smaller central portion, the necking is more prominent in the T-ET specimen which was tested at 400 °C. The cracks have appeared to initiate from the grain boundary α (α_{GB}) and have propagated along the prior

β grain boundary resulting in α - cleavage or lamellar fracture. As the prior β grains are parallel to the build direction, the fracture along the grain boundary causes the deflection of cracks at the prior β grain boundaries, resulting in a torturous crack path and a rougher central portion, as marked in Fig. 9(a) and (e) [29–31].

The flat central portion, seen in Fig. 9(b) and (f), is characterised by micro-void coalescence, resulting in a dimpled appearance, cleavage facets, numerous small opened—up pores and craters. The ductile tearing associated with the coalescence of pores is much more prominent in the fractured T-ET specimen. The irregular shaped voids with sharp edges and random orientation are also evident, which are the preferential sites for crack initiation and growth causing tearing of specimens under tensile loading as depicted in the fractured T-RT specimen as seen in Fig. 9(c). Furthermore, the T-RT specimen shows equiaxed shallow dimples appearing on the surface of the terraces as depicted in Fig. 9(d). In contrast, as observed in Fig. 9(g) and (f), the cone shaped craters caused by the larger sized pores and a spongy textured surface with numerous finer and deeper dimples suggests a greater extent of plastic deformation and ductility in the T-ET specimen.

The columnar prior β grains, α′ grains and grain boundary α (α_{GB}) can also influence the ductility of LPBF Ti—6Al—4V. The α_{GB} is softer than the α′ grains and is the prime site for damage accumulation [30]. Under tensile deformation, the strain mainly localises in α′ grains, and those α′ grains which are oriented 45° from the loading direction are the prime sites for this localisation. The boundaries of α′ grains are particularly prone to interface plasticity to accommodate strain incompatibilities with the surrounding grains/microstructure [10,29,30]. Strain localisation results in void formation within the α′ grains which subsequently results in final fracture of the material, which is a mixture of ductile and brittle fracture, where the fracture surface contains both dimples and cleavage features, a failure mechanism which has also been
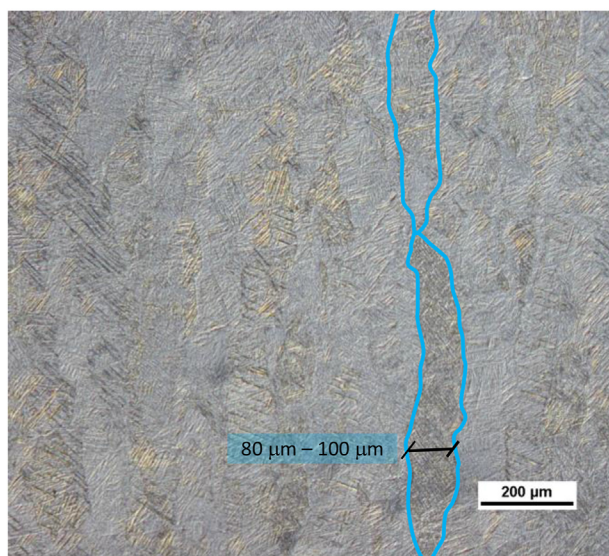
Fig. 7 — Optical micrograph of the as-built LPBF Ti—6Al—4V material, section along the build direction
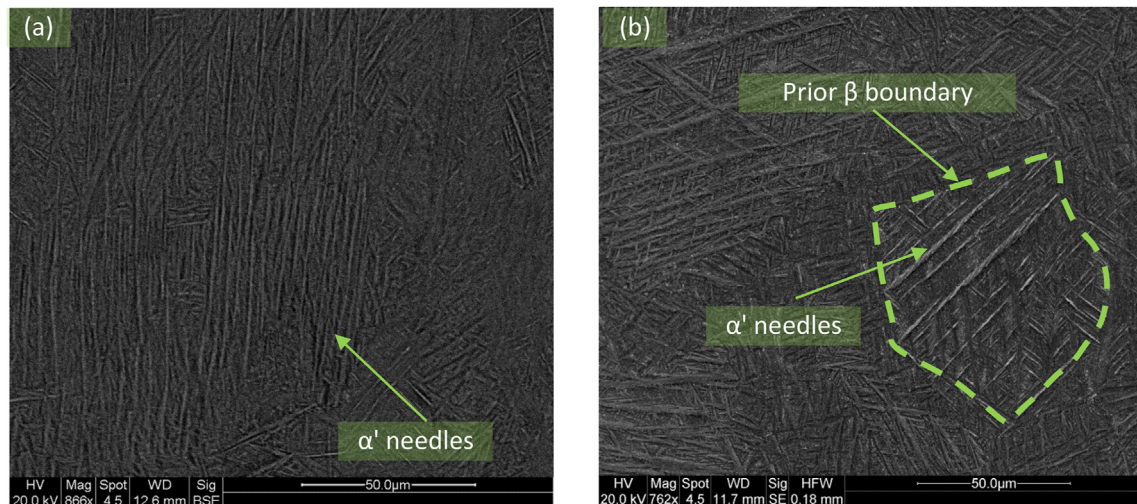
Fig. 8 – SEM micrographs showing α′ needles within the prior β grain boundary: (a) SEM image of the section containing build direction and (b) SEM image of the transverse section

observed in other studies [10,29–31]. Furthermore, the micro-voids appearing between the layers results in weaker bonding of layers which, under the action of tensile loading, open-up and subsequently grow and coalesce leading to a reduction in the ductility of LPBF Ti–6Al–4V [10]. Thus, the presence of micro-voids (size and distribution) has a negative effect on the ductility of LPBF Ti–6Al–4V.

3.3.2.2. *LCF fractured specimens.* A material subjected to LCF at high SR typically has a poorly defined Stage 1 with indications of crack initiation [14], whereas most of the crack growth happens during the Stage 2 stabilised softening region. The SEM micrographs of the fractured LCF specimens were taken to analyse the crack initiation sites and area of crack propagation, and to also understand its relationship with the cyclic softening, see Fig. 10. The test specimens L-RT3, L-ET3, L-ET2 and L-ET5 were chosen for fracture surface examination and their micro-graphs are shown in Fig. 10(a)-10(c), Fig. 10(d)-10(f), Fig. 10(g)-10(i) and Fig. 10(j)-10(l), respectively.

A higher SR in Stage 2 provokes initiation of fatigue cracks, but with the subsequent decrease in stress caused by the cyclic softening in Stage 2, this slows down the crack propagation, as depicted in Fig. 10(a), (d), 10(g) and 10(j). The crack propagation zone is defined either by a central oval/circular region for the RT test in Fig. 10(a) or by a semi-circular region for the ET tests in Fig. 10(d), (g) and 10(j). The crack initiation is either from the defects present (a pore or a void) located at the surface, observed in Fig. 10(b), (e) and 10(k), or just inside the surface of the test specimen as observed in Fig. 10(h) [13]. A small lump of material on the surface, formed due to incomplete melting during manufacturing, which would also have acted as a stress raising feature, was also observed in Fig. 10(c). Initiation of secondary micro-cracks from such a feature during cyclic loading cannot be ruled out. The fracture surface of LCF specimens does not exhibit ductile dimples or necking because of the cyclic loading and crack propagation. The region of crack propagation shows beach marks, which are typical of cyclic crack growth and are clear for ET test

specimens in Fig. 10(f), (i) and (l). The crack propagation region of ET specimens is much rougher and smaller compared to the RT specimen. A rougher surface typically indicates a torturous crack path and greater contribution of the microstructural features i.e. α lamellae, $α_{GB}$ and prior β grain boundaries. Hence the observed rougher fracture surfaces of the ET specimens indicate a higher degree of torturous deformation in these specimens. In LPBF Ti–6Al–4V, the effective slip length is confined within a single α′ grain, therefore the α′ grains are the preferential sites for initiation of cracks during cyclic loading and the crack propagation is highly dependent on the crystallographic orientation of the α′ grains [10,32]. In a fine microstructure, the advancing crack tip deviates at the grain boundaries generating predominantly intergranular features because the neighbouring α′ grains (or colonies) have multiple distinct crystallographic orientations (i.e weak texture), see section 3.4 [32]. From Fig. 10, the observed rougher crack propagation regions in the fracture surfaces in the presence of prior β grain boundaries in the microstructure (as shown in Fig. 7) confirm that the primary mode of fatigue fracture is intergranular [33].

Finally, the portion outside of the crack propagation region marked as Lip/Final Fracture is formed during the final fracture stage of the cyclic tests, see Fig. 10(a) and (d), 10(g) and 10(j). The Lip part of the fracture surfaces happens due to an increased stress (under plane stress condition) with reduced cross-sectional area in the final fracture stage and happens at an angle to the crack propagation surface area/loading axis.

3.4. EBSD mapping analysis

The key microstructural features and the phases present in the as-built LPBF Ti–6Al–4V were studied using EBSD as shown in Fig. 11. Only a small amount of β phase (~0.253%), indicated by red zones, was present. The remaining portion was the martensitic α′ phase Indicated by blue/white zones. The β phase improves ductility due to slip transfer at the α'/β interfaces [32], and a limited volume fraction of β phase
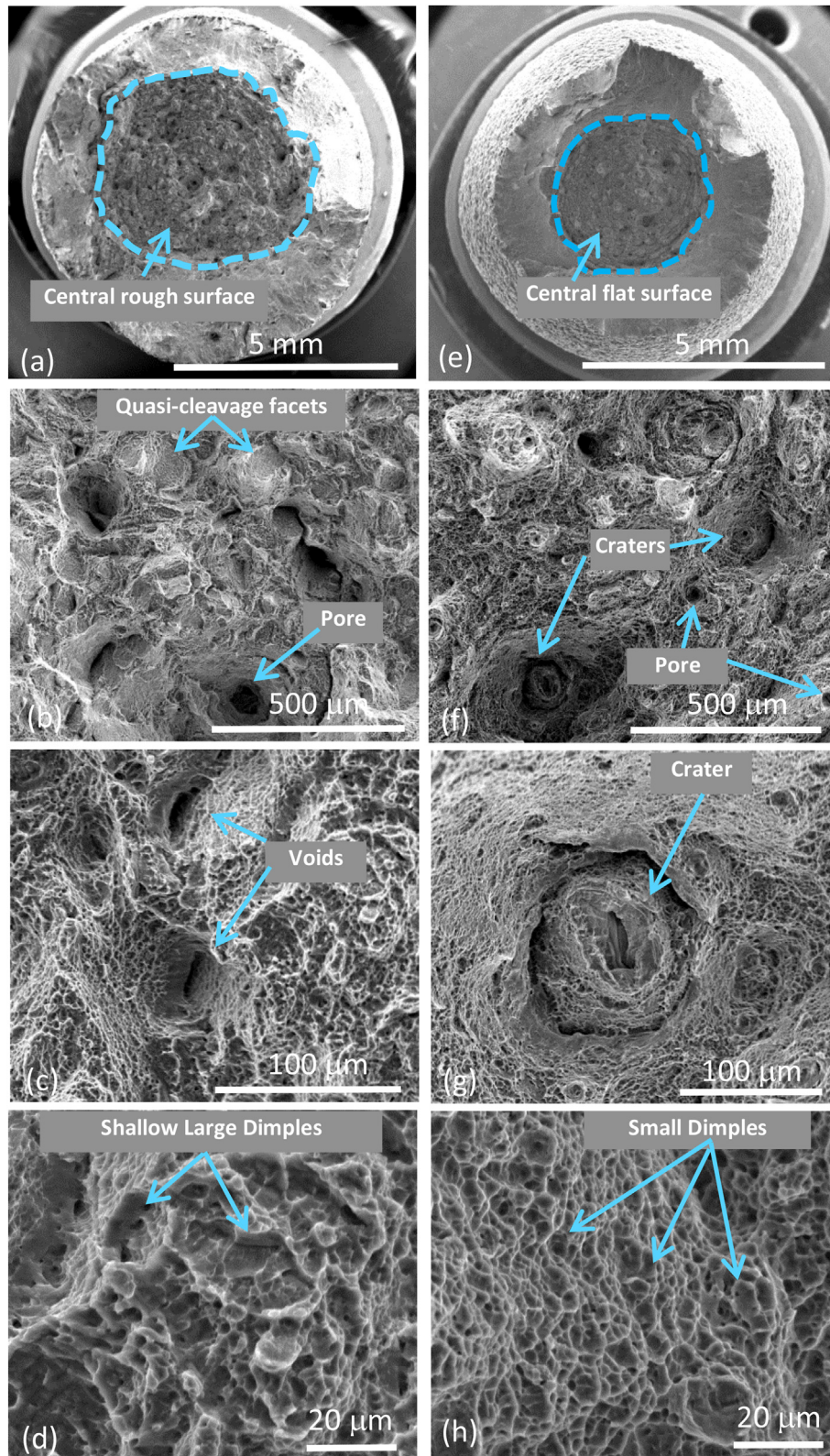
Fig. 9 — Macro and micrographs of fractures surface of tensile specimens tested at: (a)–(d) 20 °C (T-RT) and (e)–(h) at 400 °C (T-ET)
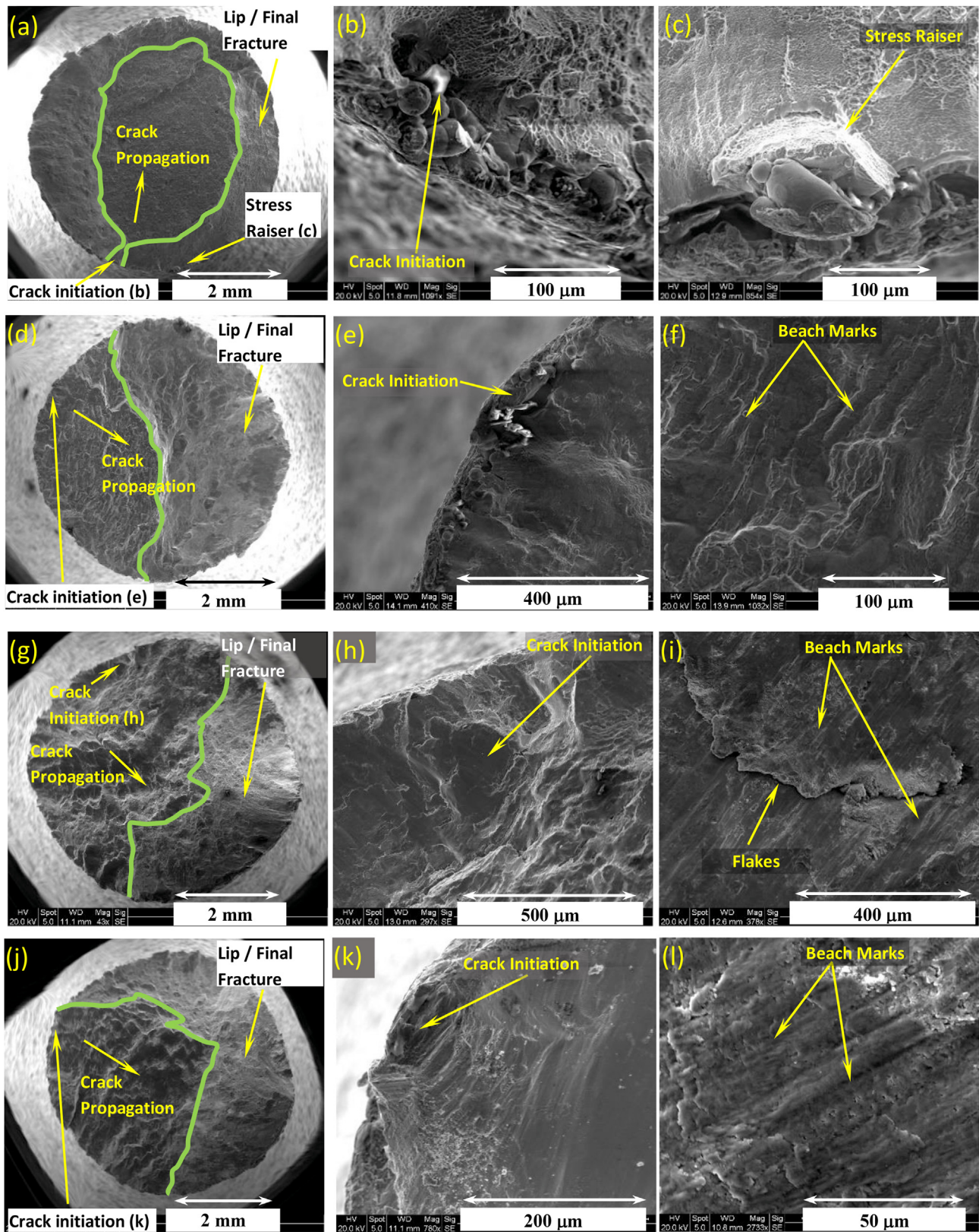
Fig. 10 — SEM micrographs of fracture surface of LCF specimens: (a)—(c) L-RT3 at temperature = 20 °C and SR = 1.5%, (d)—(f) L-ET3 at temperature = 400 °C and SR = 1.5%, (g)—(i) L-ET2 at temperature = 400 °C and SR = 1.2%, and (j)—(l) L-ET5 second interrupted test at temperature = 400 °C and SR = 1.2%
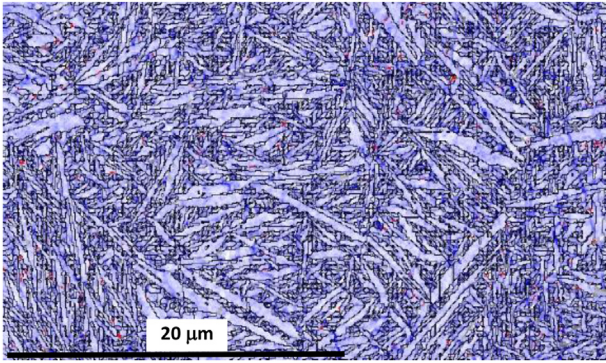
Fig. 11 – EBSD micrograph of the LPBF Ti–6Al–4V sample longitudinal-section showing grain boundary and phases present (β phase is in red and α′ is in blue/white).

suggests a relatively low ductility of the stress relieved LPBF Ti–6Al–4V as observed the T-RT tensile test (Table 5).

The Inverse Pole Figure (IPF) maps of the α phase (Ti-Hex) are shown in Fig. 12. The microstructure of LPBF Ti–6Al–4V is characterised by the columnar prior β grains with acicular α′ formed within the prior β grains [9,10] as seen in Fig. 12(a).

According to the Burgers Orientation Relationship (BOR), twelve possible orientations, referred to as variants, are formed during β phase (bcc structure) transformation to α′ [9–11,34].

BOR : $\{110\}_\beta \big\| \{0001\}_\alpha$ (parallel planes) and

$\langle 111 \rangle_\beta \big\| \langle 11\bar{2}0 \rangle_\alpha$ (parallel direction)

Several α′ needles of the same variants may give rise to the colonies of α′ in the microstructure as observed in the same colour in Fig. 12(a). The columnar prior β grains with strong texture of ⟨1 0 0⟩ build direction enhances the anisotropy of the mechanical strength and fatigue properties. However, the acicular α′ needles, with their long axis confined within the prior β grain boundaries and different variants distributed uniformly (see Fig. 12(a)), promotes the material to behave in an isotropic manner [9]. The thickness of α′ relies on the processing parameters and resulting thermal history, and the post processing heat treatments. The reduced thickness of α′
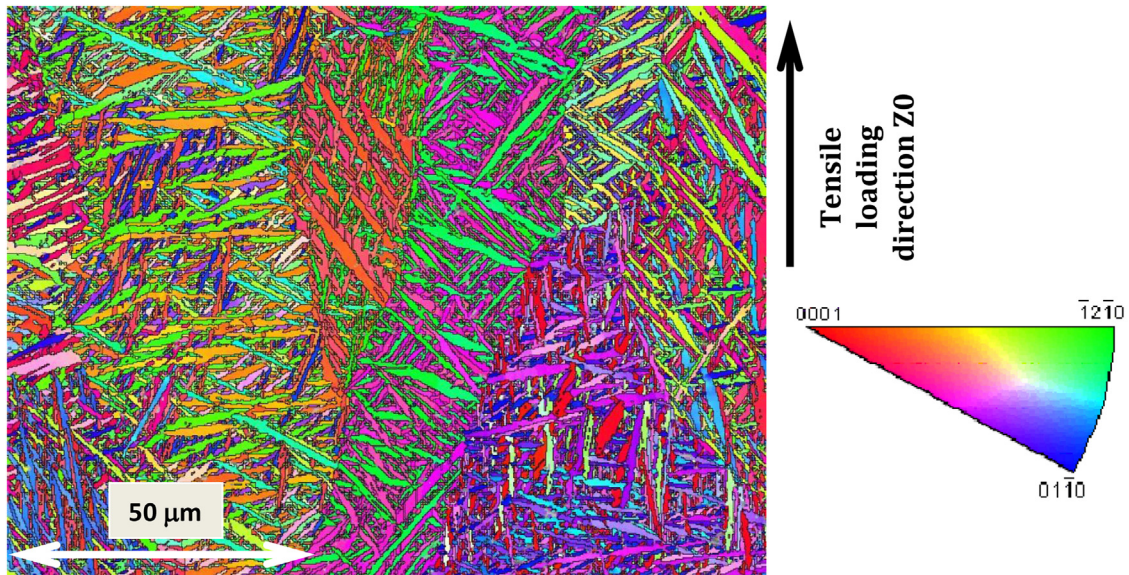
(a)
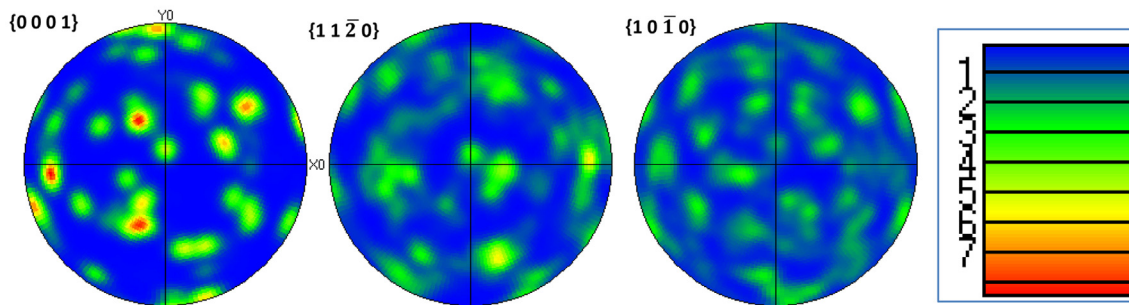
(b)

Fig. 12 – EBSD images of LPBF Ti–6Al–4V sample, cross-section parallel to the build direction: (a) IPF Z0 map revealing crystallographic orientation, and (b) Crystallographic texture pole figures

grains tends to improve the monotonic strength of LPBF Ti—6Al—4V compared to the wrought Ti—6Al—4V, as seen in this study [32,34]. Hence, typically a finer grain size (α' and β) is desired by the end users to achieve higher mechanical strength of LPBF Ti—6Al—4V [9].

As the volume fraction of β-phase is small, only the texture of the α' phase was studied using the IPF map shown in Fig. 12(b). Crystallographic grains in red indicate that the α' needles are oriented towards (0001) basal planes and there was no obvious local preferred orientation of the α' phase microstructure. The pole intensity of the basal planes $\{0\,0\,0\,1\}_\alpha$, aligned parallel to the build direction (Z_0 axis in pole figures), showed the strongest absolute textures of the α' phase, whereas the $\{1\,0\,\bar{1}\,0\}_\alpha$ prismatic plane pole figures showed the weakest texture.

4. Discussion

4.1. Evolution of Low Angle Boundaries (LABs) and increase in free dislocation density

The softening observed in the strain controlled cyclic tests causes crack growth retardation from subsequent primary or secondary cracks, often resulting in a better fatigue life when compared to stress-controlled LCF tests [13]. The dislocation activities, including activation of multiple slip systems and the increase in free dislocation density within the α' grains, play a significant role in the overall cyclic deformation behaviour [16]. The α' needles, which have a high aspect ratio, are the soft features in the microstructure where long dislocations mean a free and weaker path in the longitudinal direction of the needles. In addition to this, a higher tendency of strain localisation is observed in the colonies of α' needles belonging to the same crystallographic orientation [10]. Moreover, the α' needles impede the growth of subsequently produced α' needles, which reduces the ability of the material to deform under the applied force but enhances material plasticity and strain localisation in the α' needles. Plastic deformation in Ti—6Al—4V is mostly accommodated by the Basal or Prismatic slip system namely (0002) ⟨1 1$\bar{2}$ 0⟩ and (1 1$\bar{1}$ 0)⟨1 1$\bar{2}$ 0⟩ [32].

The distribution of strain within the material microstructure is typically studied using a KAM distribution map which signifies the free dislocation density distribution in a deformed material. In a KAM distribution map of a deformed or strained material, any area with a high KAM number would correspond to an area of high free dislocation density/high local strain [35]. On the contrary, a low KAM value would typically suggest that the primary deformation mechanism is due to grain boundary sliding rather than the sub-grain formation [35].

The specimens were investigated to further study the cyclic softening behaviour and any dependency on the evolution of grain size and free dislocation density as indicated by the KAM. For this, a comparative study was performed using the results of EBSD scans performed on the longitudinal cut sections of the as-received LPBF Ti—6Al—4V, and the L-ET2, L-ET4 and L-ET5 tested specimens. The L-ET4 and L-ET5 were the two interrupted tests at ET with a SR of ±1.2%, see Table 6.

Firstly, the test points (P1 — P4) for microstructure evolution study are identified on a normalised softening curves in Fig. 13, where P1 is the as-received LPBF Ti—6Al—4V condition and P4 is the fracture point of the baseline L-ET2 test. Although the interrupted tests (L-ET4/P2 and L-ET5/P3, see Table 6 and Fig. 13)) were individually planned to be stopped at a predetermined number of cycles without fracture, the second interrupted test specimen (L-ET5) fractured prematurely. Also, the L-ET5 test was observed to have lower starting stress compared to the baseline L-ET2 test. Therefore, the softening curves were normalised to identify the relative positions of the end points of the two interrupted tests, and also to relate and ensure that the softening trends of the interrupted tests followed the softening trend of the baseline L-ET2 test. The end of the first interrupted test (L-ET4) P2, which was stopped after 160 cycles falls in the stabilised part, i.e. in Stage 2, of the softening curve of the baseline L-ET2 test, see Fig. 13. The end of the second interrupted test, P3, falls in Stage 3, representing the accelerated softening part of the softening curve of the baseline L-ET2 test. As shown in Fig. 13., both the interrupted tests seem to closely follow the softening trend of the baseline curve.

For the points P1 — P4, shown in Fig. 13, a comparison of EBSD results between the as-built LPBF Ti—6Al—4V (P1) and fatigued samples from the L-ET4 (P2), L-ET5 (P3) and L-ET2 (P4) tests is shown in Fig. 14 using the IPF plots (Z0, loading axis) and KAM plots. For the fatigued specimens, two locations were studied, where location 1 was 1 mm away from the fractured/cut surface and location 2 at the fractured/cut surface. The IPF plots in Fig. 14 show a continuous refinement of α' grains with fatigue cycles increasing from P1 to P4. The
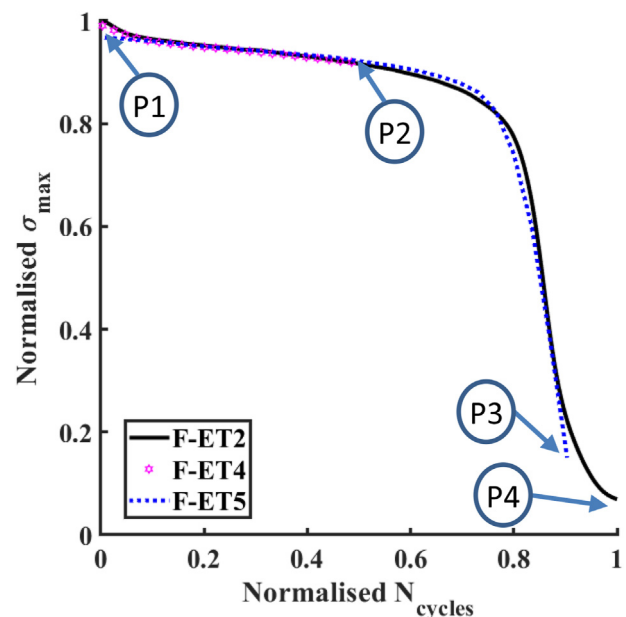
Fig. 13 — Normalised softening response curves of the interrupted tests (L-ET4 and L-ET5) relative to baseline test (L-ET2). Points P1, P2, P3 and P4 represent the as -built Ti—6Al—4V material, end of the interrupted test L-ET4, end of the interrupted test L-ET5 and end of the baseline L-ET2 test
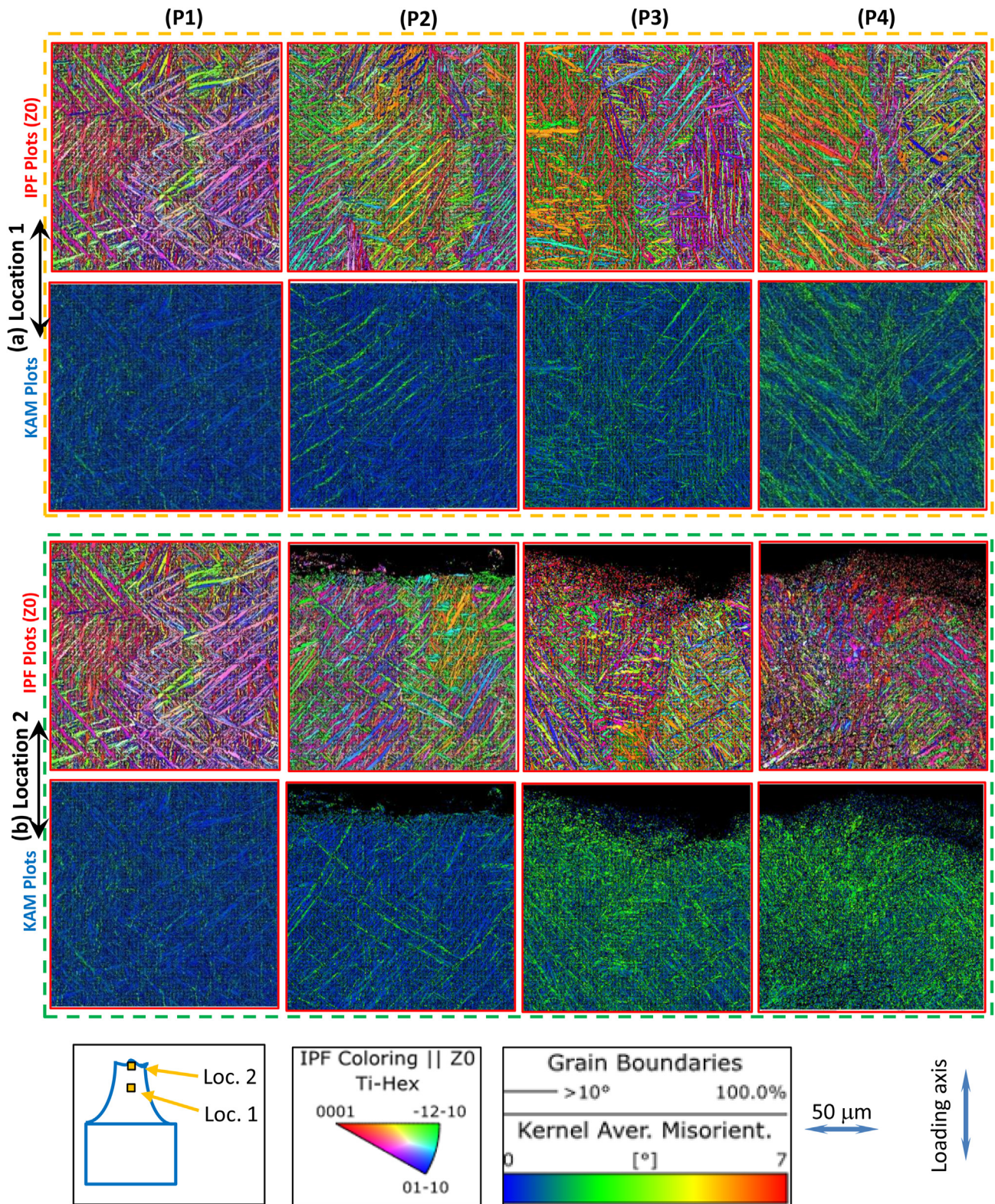
Fig. 14 – Comparison of EBSD results between the as-built LPBF Ti−6Al−4V material (P1) and fatigued samples from the L-ET4 (P2), L-ET5 (P3) and L-ET2 (P4) tests with IPF plots and KAM maps. For fatigued specimens, two locations were studied where location 1 is 1 mm away from the fractured/cut surface and location 2 is at the fractured/cut surface

Table 7 – A comparison of average KAM values (°) between the as-built sample and LCF tested specimens.

| Test Identification Number (#)	Location Description	Test Point Description	Average KAM (°)
–	As-built LPBF Ti–6Al–4V	P1	0.8
L-ET4	Location 1	P2	0.8
L-ET5		P3	0.98
L-ET2		P4	1.15
L-ET4	Location 2	P2	0.87
L-ET5		P3	1.43
L-ET2		P4	1.59

degree of grain refinement is greater for location 2 (close to the fracture surface) compared to location 1. Also, as seen in Fig. 14, the fatigued samples (P2 –P4) show moderate to high KAM values (shown in green), with an increase in the number of fatigue cycles (P2 to P4) and which are spread throughout the microstructure of the scanned area, compared to the as-built sample (P1). The fatigued microstructure is comprised of a uniform distribution of sub-grains and KAM density, i.e. dislocations are homogenously distributed inside the larger α' grains. The average KAM values for each of the scanned area in Fig. 14 are listed in Table 7, which indicate that the average KAM increases as we move from P1 to P4 and from locations 1 to 2 (i.e at the fracture surface).

During deformation, evolution of dislocation substructures takes place in LPBF Ti–6Al–4V and this subsequently produces Low Angle Boundaries (LABs) inside the prior α/α' grains [10,36]. A misorientation less than 15° between two adjacent entities (grains or sub-grains) in the microstructure usually results from the formation of LABs whereas a mis-orientation higher than 15° provided information on the well-defined α' grain boundaries. The LABs apapear to originate from the interface of α, β phases which do not follow the said BOR

between the β and α phases [36]. The generation of LABs is through the formation of dislocation tangles and subsequent recovery leading to rearrangement of dislocations during cyclic loading. The LABs are therefore composed of an array of dislocations, which can be of edge or screw types; these progressively lead to void nucleation, coalescence, and fracture [35]. Usually, the dislocations do not exist inside the sub-grains.

From the discussion above, the free dislocation density increases with increasing number of LCF cycles, due to a combination of: (i) easing of dislocation annihilation and (ii) recovery of dislocations happening subsequently. Typically, a substructure with distributed dislocation density within the material would undergo plastic deformation through dislocation motion. Moreover, the cyclic softening occurs due to an increasing dislocation density, decreasing the density of obstacles to dislocation motion and increasing the ability of dislocations to overcome these obstacles [37]. Furthermore, an increase in the free dislocation density also helps to cause initiation of cracks in the bulk of material, contributing to the LCF fatigue damage in the Ti–6Al–4V [38].

To relate the cyclic softening to the material hardness, microhardness mapping was performed on a longitudinal section of the as-built LPBF Ti–6Al–4V (P1) and of the fatigued samples of L-ET4 (P2), L-ET5 (P3) and E-ET2 (P4) tests. These microhardness results are shown in Fig. 15, where it can be seen that the average indicative microhardness value appears to increase with the increasing number of cycles (from P1 to P4 of the cyclic tests). In the cyclic LCF tests studied, with the increasing number of cycles, the stress amplitude decreases (cyclic softening) because of the increased occurrences of <c + a> slips (in addition to increase in free dislocation density). The increased occurrence of <c + a> slip enhances the interaction of <a>/<c + a> and <c + a>/<c + a> dislocations which then generates latent hardening to counter balance the cyclic
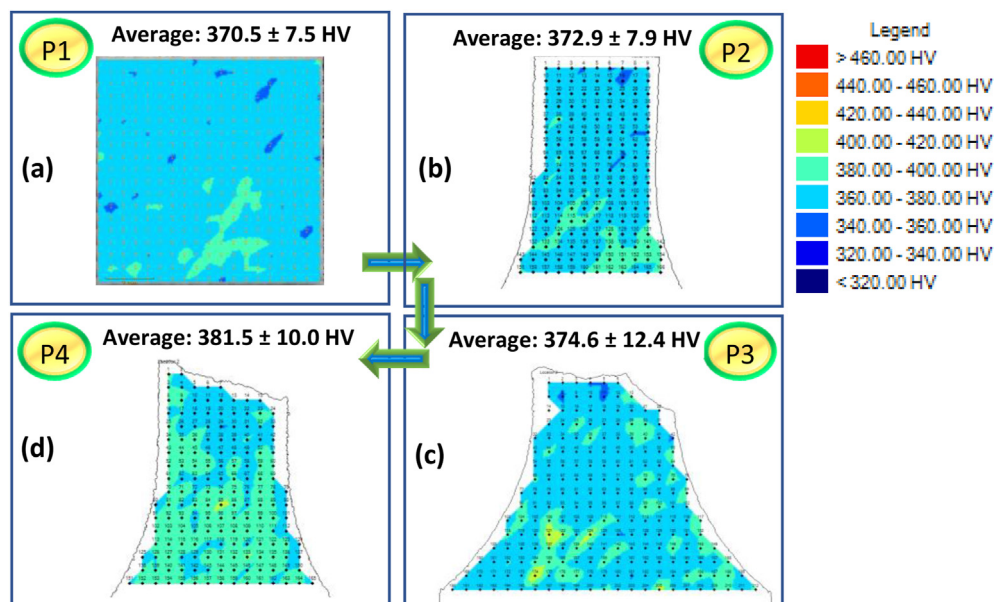
Fig. 15 – Hardness tests results of: (a) as-built LPBF Ti–6Al–4V alloy (P1), (b) fatigued sample of L-ET4 test (P2), (c) fatigued sample of L-ET5 test (P3), and (d) fatigued sample of L-ET2 test (P4)
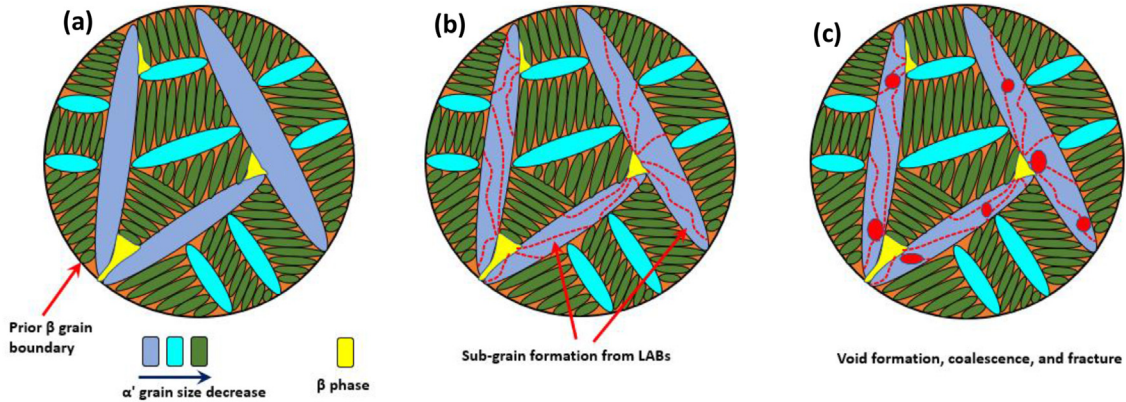
Fig. 16 – A schematic representation evolution of LABs: (a) α′ grains within prior β grain boundaries, (b) formation of sub-grains within α′ grains due to dislocation activities and interfacial plasticity, and (c) formation of voids and void coalescence and propagation till fracture under the effect of cyclic loading [10]

softening to some extent [15]. Here c and a denote the lattice parameters of a hexagonal closed packed unit cell [11]. It should be noted that the microhardness of the as-built LPBF Ti−6Al−4V shows a higher micro-hardness value (370 HV

average measured with a load of 500 gf, P1 in Fig. 15), due to its fine microstructure with α′ needles, compared to the extruded equiaxed α/β Ti−6Al−4V (302 HV average measured with a load 1000 gf [39], suggesting that the as-built LPBF Ti−6Al−4V
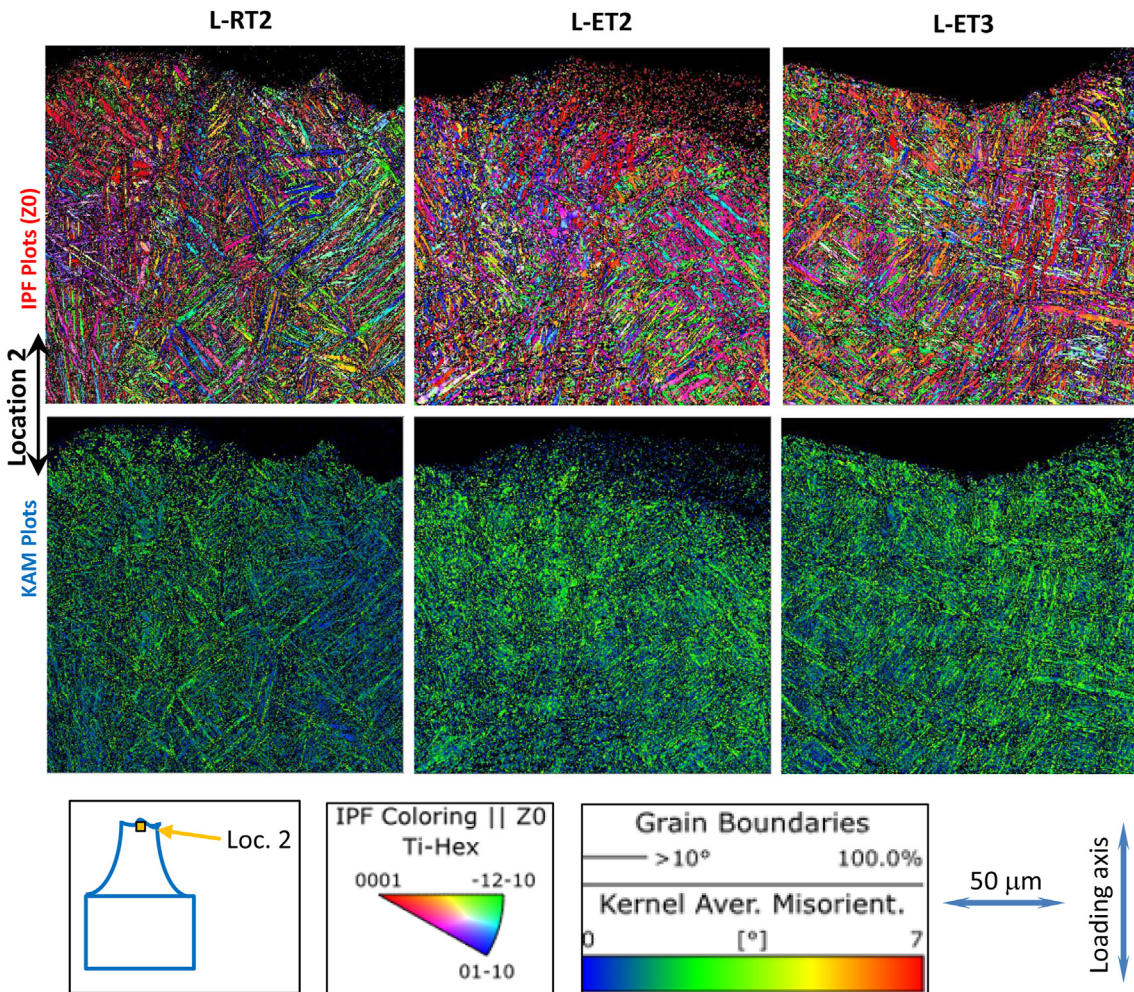
Fig. 17 – Comparison of EBSD results between the fatigued samples from the L-RT2, L-ET2 and L-ET3 tests with IPF plots and KAM maps. Only the scans at the fractured surface (location 2)

Table 8 – Effect of temperature and strain range under cyclic loading: A comparison of average KAM values (°).

Test Identification Number (#)	Temperature (°C)	Strain Range (SR) (%)	Average KAM (°)	Cycles to Failure
L-RT2	20	±1.2	1.38	294
L-ET2	400	±1.2	1.59	319
L-ET3	400	±1.5	1.68	144

is, in general, harder than the conventionally made Ti–6Al–4V).

As discussed in section 3.1.1., the ductility of LPBF Ti–6Al–4V increases at ET. Hence, based on the discussion above, the increase in free dislocation density, local strengthening (hardness) and ductility results in micro-void formation and their coalescence, eventually leading to fracture under cyclic loading at ET. A schematic representation of the evolution of LABs due to progressive dislocation interaction and formation of voids leading to cyclic fracture is shown in Fig. 16 [10].

### 4.2. Effect of temperature and strain range

Again, the LPBF Ti–6Al–4V, subjected to cyclic loading at ET, will undergo microstructural evolution and dislocation activity (an increase in both dislocation density and ease of dislocation motion) leading to significant cyclic softening [14]. The effects of SR and temperature were studied by comparing the

IPF and KAM plots of the fatigued samples of L-RT2, L-ET2 and L-ET3 at location 2 only, as shown in Fig. 17. It can be seen that the orientation of grains is homogenous for all three fatigued specimens. The grains of the ET test specimens (L-ET2 and L-ET3) are much finer compared to the grain size observed for the fatigued sample of the RT test (L-RT2). The distribution of KAM (indicated by the fact that green is much more prominent for the ET tests when compared to the RT test (L-RT2 vs. L-ET2) and the KAM increases further with increasing test SR (L-ET2 vs. L-ET3). The average KAM values for the three tests for the scanned area in Fig. 17 are also tabulated in Table 8. For the tests at ET (see Table 8), as expected, the average KAM increases with increasing SR and the cycles to failure decreases (L-ET2 vs. L-ET3). However, between the L-RT2 and L-ET2 tests, although the KAM increases with the increase in temperature, the number of cycles to failure decreases. Furthermore, From Fig. 5, the hysteresis loops for tests at ET exhibit higher slope in the tensile part of the hysteresis loop compared to the slope of compression part, suggesting that the material experiences a faster crack growth under the tensile part of the loading cycle. This confirms a parallel and competing contribution of strain localisation, micro-hardness, micro-voids, coalescence of micro-voids and rate of crack growth towards fracture of the specimens.

The cyclic softening intensifies with the increase in SR as seen in Figs. 4 and 5. The increase in plasticity levels helps towards the free dislocation density pile-up and thus accelerates the cyclic softening rate. In addition to dislocation pile-ups at higher SR, under the cyclic loading at ET, the interaction between the dislocations increases, which in-turn reduces the
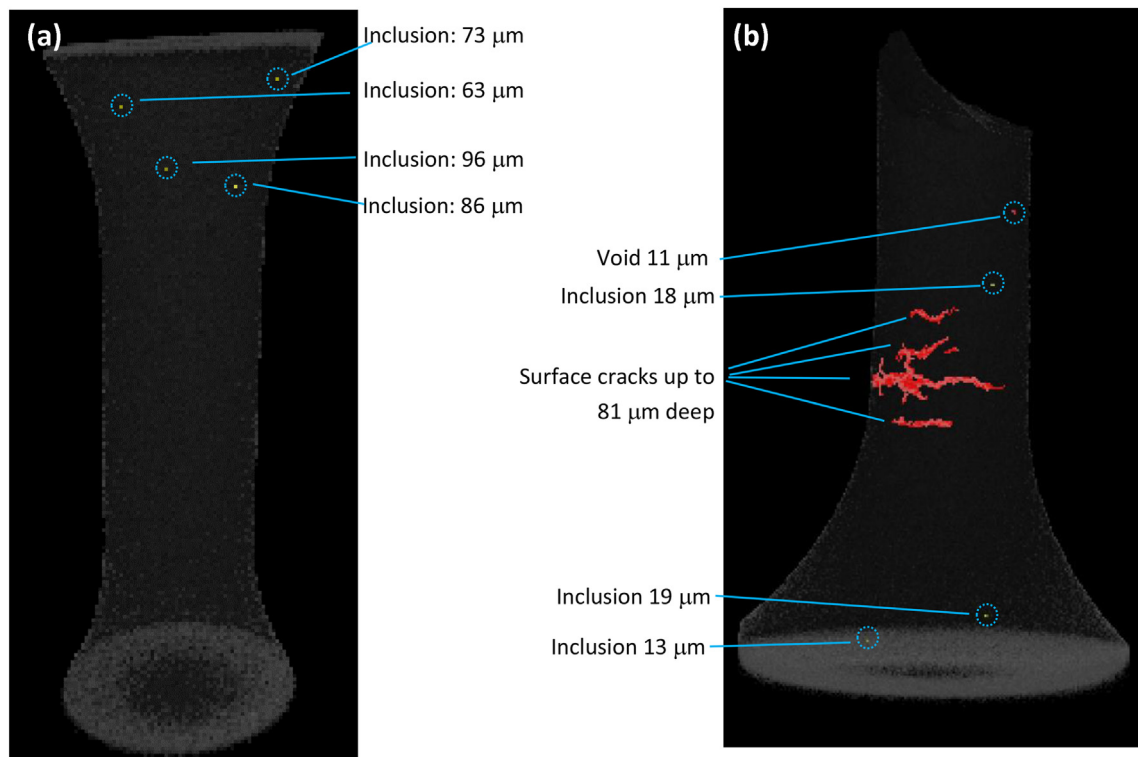
Fig. 18 – CT scanning of LCF tested specimens (a) L-ET4 specimen showing presence of inclusions, and (b) L-ET5 specimen showing inclusions, micro-voids and propagating cracks
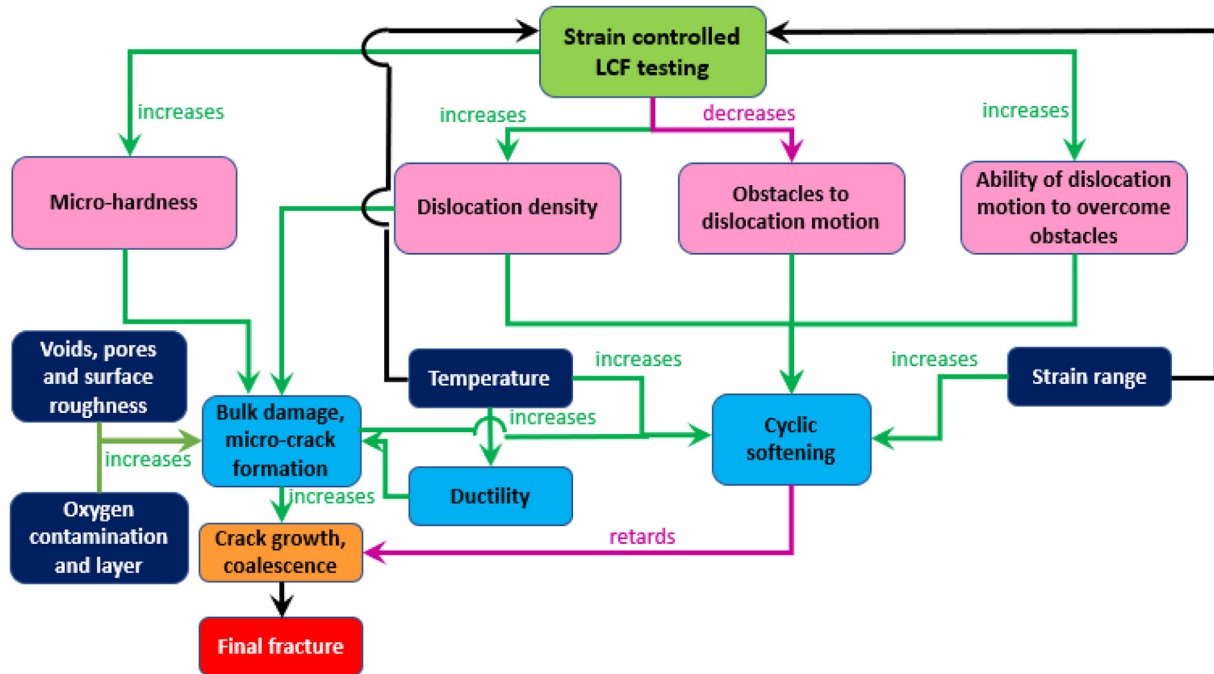
Fig. 19 — Strain controlled LCF test performance of Ti—6Al—4V - A diagram illustrating complex interaction of various parameters

obstacles to dislocation motion and increases the ability of material to overcome these obstacles to dislocation motion, which then results in a significantly higher cyclic softening until final fracture, compared to the RT tests.

4.3. Defects in LCF tested samples

Post LCF testing, CT scanning was performed on the L-ET4 and L-ET5 test specimens which were used for the two interrupted tests. The 3D constructed CT images for these two specimens are shown in Fig. 18. It can be seen in Fig. 18(a) that the L-ET4 specimen consisted of only 4 inclusions with a maximum size of 96 μm; however, the L-ET5 specimen was found to have inclusions (maximum 19 μm size), micro-voids (maximum 11 μm size) and surface nucleating cracks (maximum 81 μm deep), as depicted in Fig. 18(b). As presented in Fig. 10(k) and also discussed in Section 3.3.2.2, the micro-voids present at the surface of L-ET5 specimen caused the crack initiation, which subsequently propagated and led to final fracture of the specimen under cyclic loading. There are other multiple cracks seen in Fig. 18(b), which initiated from the surface of the L-ET5 specimen and propagated within the material. These cracks although not resulting in a complete fracture would have reduced the load carrying capability of the material, due to reduction in cross-sectional area available to take the applied load. This suggests that the micro-voids or pores in the LPBF material could lead to premature failure.

Furthermore, the lack of fusion voids or pores present at or near the surface and microcracks present at the rough surface are detrimental (compared to the buried defects in the bulk of the material), and typically act as the crack initiation points which propagate to cause fracture of the LPBF specimens/ components under the LCF loading (see Fig. 10).

4.4. Additional considerations

To improve fatigue life of LPBF Ti—6Al—4V, the goal should be to reduce the occurrence of these micro-voids and also their sizes, using the optimal build parameters and also by using the HIP process. Additionally, the use of post-build machining to improve the surface roughness, which thereby removes the surface nucleating micro-cracks, pores and voids, will improve the fatigue life of the LPBF parts [40,41]. However, the machining and HIP processes are expensive and at the same time negatively impact the lead time of LPBF parts to reach to the customer [40,41]. Therefore, practicing design and manufacturing engineers should put their efforts into optimising the product design and manufacturing with optimal build parameters, so that the end use of LPBF Ti—6Al—4V parts come without these costly additional processes. Based on the discussion above, the influence of various different parameters on LCF performance of LPBF Ti—6Al—4V, including cyclic softening and crack growth, is summarised on the interaction diagram shown in Fig. 19.

Furthermore, the LCF response of LPBF Ti—4Al—4V is also likely to be dependent upon the strain rates used during the LCF testing [42]. In the current study, the effect of varying strain rate was not explored due to the constraints related to time and resources, but it is suggested that this effect is explored as part of the future research studies.

5. Conclusions

To evaluate the mechanical strength and LCF performance of the LPBF Ti-6AL-4V, tensile and strain controlled LCF tests at

different SRs were carried out at RT (20 °C) and ET (400 °C). The following conclusions can be made based on this study:

- LPBF Ti—6Al—4V has greater tensile strengths (PS and UTS) than conventionally manufactured wrought Ti—6Al—4V, due to its microstructure with fine α′ needles, which provide small slip lengths. At ET, the material strength decreased due to the reduction in resistance to plastic flow, but the ductility increased.

- Cyclic softening was observed in each of the LCF tests and RT and ET. For cyclic tests at ET, the LPBF Ti—6Al—4V exhibited higher cyclic softening, compared to cyclic tests at RT, which was due to higher interaction of dislocations and faster crack growth under tensile part of the cyclic loading in cyclic tests at ET.

- During cyclic deformation, the evolution of dislocation substructures takes place to subsequently produce LABs inside the prior α′ grains. The LABs progressively lead to nucleation and coalescence of voids with fatigue cycles, eventually leading to fracture.

- With an increase in fatigue cycles, an ease of dislocation annihilation and subsequent recovery of dislocations happens, which causes the free dislocation density to increase and results into cyclic softening of LPBF Ti—6Al—4V. Also, with higher test SR, the free dislocation density increases.

- The lack of fusion voids or pores, present at or near the surface, and microcracks, present at the rough surface, act as crack initiation locations which propagate to cause fracture of the LPBF specimens/components under LCF loading, where the primary mode of fatigue fracture observed is intergranular.

Declaration of Competing Interest

The authors declare that they have no known competing financial interests or personal relationships that could have appeared to influence the work reported in this paper.

Acknowledgements

REFERENCES

[1] Hu YN, Wu SC, Wu ZK, Zhong XL, Ahmed S, Karabal S, et al. A new approach to correlate the defect population with the fatigue life of selective laser melted Ti-6Al-4V alloy. Int J Fatig 2020;136. https://doi.org/10.1016/j.ijfatigue.2020.105584.

[2] Javidrad HR, Ghanbari M, Javidrad F. Effect of scanning pattern and volumetric energy density on the properties of selective laser melting Ti-6Al-4V specimens. J Mater Res Technol 2021;12:989—98. https://doi.org/10.1016/j.jmrt.2021.03.044.

[3] Nguyen HD, Pramanik A, Basak AK, Dong Y, Prakash C, Debnath S, et al. A critical review on additive manufacturing of Ti-6Al-4V alloy: microstructure and mechanical properties. J Mater Res Technol 2022;18:4641—61. https://doi.org/10.1016/j.jmrt.2022.04.055.

[4] Chowdhury S, Yadaiah N, Prakash C, Ramakrishna S, Dixit S, Gupta LR, et al. Laser powder bed fusion: a state-of-the-art review of the technology, materials, properties & defects, and numerical modelling. J Mater Res Technol 2022;20:2109—72. https://doi.org/10.1016/j.jmrt.2022.07.121.

[5] Hu YN, Wu SC, Withers PJ, Zhang J, Bao HYX, Fu YN, et al. The effect of manufacturing defects on the fatigue life of selective laser melted Ti-6Al-4V structures. Mater Des 2020;192. https://doi.org/10.1016/j.matdes.2020.108708.

[6] Guleryuz H, Cimenoglu H. Oxidation of Ti-6Al-4V alloy. J Alloys Compd 2009;472:241—6. https://doi.org/10.1016/j.jallcom.2008.04.024.

[7] Lütjering G. Influence of processing on microstructure and mechanical properties of (α+β) titanium alloys. Mater Sci Eng 1998;243:32—45. https://doi.org/10.1016/S0921-5093(97)00778-8.

[8] Bao J, Wu S, Withers PJ, Wu Z, Li F, Fu Y, et al. Defect evolution during high temperature tension-tension fatigue of SLM AlSi10Mg alloy by synchrotron tomography. Mater Sci Eng 2020;792:139809. https://doi.org/10.1016/j.msea.2020.139809.

[9] Yang Y, liu YJ, Chen J, Wang HL, Zhang ZQ, Lu YJ, et al. Crystallographic features of α variants and β phase for Ti-6Al-4V alloy fabricated by selective laser melting. Mater Sci Eng 2017;707:548—58. https://doi.org/10.1016/j.msea.2017.09.068.

[10] Moridi A, Demir AG, Caprio L, Hart AJ, Previtali B, Colosimo BM. Deformation and failure mechanisms of Ti—6Al—4V as built by selective laser melting. Mater Sci Eng 2019;768. https://doi.org/10.1016/j.msea.2019.138456.

[11] Beladi H, Chao Q, Rohrer GS. Variant selection and intervariant crystallographic planes distribution in martensite in a Ti-6Al-4V alloy. Acta Mater 2014;80:478—89. https://doi.org/10.1016/j.actamat.2014.06.064.

[12] Molaei R, Fatemi A, Sanaei N, Pegues J, Shamsaei N, Shao S, et al. Fatigue of additive manufactured Ti-6Al-4V, Part II: the relationship between microstructure, material cyclic properties, and component performance. Int J Fatigue 2020;132. https://doi.org/10.1016/j.ijfatigue.2019.105363.

[13] Bressan S, Ogawa F, Itoh T, Berto F. Cyclic plastic behavior of additively manufactured Ti-6Al-4V under uniaxial and multiaxial non-proportional loading. Int J Fatig 2019;126:155—64. https://doi.org/10.1016/j.ijfatigue.2019.05.003.

[14] Ren YM, Lin X, Guo PF, Yang HO, Tan H, Chen J, et al. Low cycle fatigue properties of Ti-6Al-4V alloy fabricated by high-power laser directed energy deposition. Experimental and prediction 2019;127:58—73. https://doi.org/10.1016/j.ijfatigue.2019.05.035.

[15] Luquiau D, Feaugas X, Clavel M. Cyclic softening of the Ti-10V-2Fe-3Al titanium alloy. Mater Sci Eng 1997;224:146—56. https://doi.org/10.1016/s0921-5093(96)10531-1.

[16] Huang J, Wang Z, Xue K. Cyclic deformation response and micromechanisms of Ti alloy Ti-5Al-5V-5Mo-3Cr-0.5Fe. Mater Sci Eng 2011;528:8723—32. https://doi.org/10.1016/j.msea.2011.08.045.

[17] Prasad K, Kumar V. Isothermal and thermomechanical fatigue behaviour of Ti − 6Al − 4V titanium alloy. Mater Sci Eng 2011;528:6263–70. https://doi.org/10.1016/j.msea.2011.04.085.

[18] Han F, Tang B, Kou H, Li J, Deng Y, Feng Y. Cyclic softening behavior of Ti−6Al−4V alloy at macro and micro-scale. Mater Lett 2016;185:115–8. https://doi.org/10.1016/j.matlet.2016.08.119.

[19] Guleryuz H, Cimenoglu H. Oxidation of Ti-6Al-4V alloy. J Alloys Compd 2009;472:241–6. https://doi.org/10.1016/j.jallcom.2008.04.024.

[20] Gaddam R, Sefer B, Pederson R, Antti M. Study of alpha-case depth in Ti-6Al-2Sn-4Zr-2Mo and Ti-6Al-4V, 7th EEIGM international conference on advanced materials research. IOP Conf Ser Mater Sci Eng 2013;48:1–9. https://doi.org/10.1088/1757-899X/48/1/012002.

[21] ASTM B348/B348M − 19. Standard specification for titanium and titanium alloy bars and billets. ASTM International; 2019. p. 1–9. https://doi.org/10.1520/B0348_B0348M-19.

[22] Guzman J, Nobre RDM, Junior DLR, et al. Comparing spherical and irregularly shaped powders in laser powder bed fusion of Nb47Ti alloy. J Mater Eng Perform 2021;30:6557–67. https://doi.org/10.1007/s11665-021-05916-9.

[23] ASTM F2971-13. Standard practice for reporting data for test specimens prepared by additive manufacturing. ASTM International; 2013. p. 1–4. https://doi.org/10.1520/F2971-13.

[24] ISO/ASTM 52921-13. Standard Terminology for Additive Manufacturing - Coordinate Systems and Test Methodologies. ASTM International; 2019. p. 1–14. https://doi.org/10.1520/ISOASTM52921-13R19.

[25] BS ISO 12106:2017. Metallic materials — fatigue testing — axial-strain controlled method, British Standard. BSI Standards Publication; 2017. 9780580902611.

[26] Li P, Guo W, Huang W, Su Y, Lin X, Yuan K. Thermomechanical response of 3D laser-deposited Ti − 6Al − 4V alloy over a wide range of strain rates and temperatures. Mater Sci Eng 2015;647:34–42. https://doi.org/10.1016/j.msea.2015.08.043.

[27] Lee WS, Lin CF. High-temperature deformation behaviour of Ti6A14V alloy evaluated by high strain-rate compression tests. J Mater Process Technol 1998;75:127–36. https://doi.org/10.1016/S0924-0136(97)00302-6.

[28] MMPDS-14. Metallic materials properties development and standardization, federal aviation administration. Battelle Memorial Institute; 2019. p. 57–122 [Chapter 5] Titanium Alloys.

[29] Carroll BE, Palmer TA, Beese AM. Anisotropic tensile behavior of Ti-6Al-4V components fabricated with directed energy deposition additive manufacturing. Acta Mater 2015;87:309–20. https://doi.org/10.1016/j.actamat.2014.12.054.

[30] Dehghan-Manshadi A, Reid MH, Dippenaar RJ. Effect of microstructural morphology on the mechanical properties of titanium alloys. J. Phys. Conf. Ser. 2010;240. https://doi.org/10.1088/1742-6596/240/1/012022.

[31] Zhao X, Li S, Zhang M, Liu Y, Sercombe TB, Wang S, et al. Comparison of the microstructures and mechanical properties of Ti-6Al-4V fabricated by selective laser melting and electron beam melting. Mater Des 2016;95:21–31. https://doi.org/10.1016/j.matdes.2015.12.135.

[32] Simonelli M, Tse YY, Tuck C. Effect of the build orientation on the mechanical properties and fracture modes of SLM Ti-6Al-4V. Mater Sci Eng 2014;616:1–11. https://doi.org/10.1016/j.msea.2014.07.086.

[33] Simonelli M, Tse YY, Tuck C. On the texture formation of selective laser melted Ti-6Al-4V. Metall. Mater. Trans. A Phys. Metall. Mater. Sci. 2014;45:2863–72. https://doi.org/10.1007/s11661-014-2218-0.

[34] Agius D, Kourousis KI, Wallbrink C, Song T. Cyclic plasticity and microstructure of as-built SLM Ti-6Al-4V: the effect of build orientation. Mater Sci Eng 2017;701:85–100. https://doi.org/10.1016/j.msea.2017.06.069.

[35] Roy S, Sarkar A, Suwas S. On characterization of deformation microstructure in Boron modified Ti-6Al-4V alloy. Mater Sci Eng 2010;528:449–58. https://doi.org/10.1016/j.msea.2010.09.026.

[36] Jha JS, Dhala S, Toppo SP, Singh R, Tewari A, Mishra SK, et al. Effect of strain amplitude on low cycle fatigue and microstructure evolution in Ti-6Al-4V: a TKD and TEM characterization. Mater Char 2019;155:109829. https://doi.org/10.1016/j.matchar.2019.109829.

[37] Bao J, Wu Z, Wu S, Withers PJ, Li F, Ahmed S, et al. Hot dwell-fatigue behaviour of additively manufactured AlSi10Mg alloy : relaxation , cyclic softening and fracture mechanisms. Int J Fatig 2021;151:106408. https://doi.org/10.1016/j.ijfatigue.2021.106408.

[38] Kamaya M. Influence of bulk damage on crack initiation in low-cycle fatigue of 316 stainless steel. Fatig Fract Eng Mater Struct 2010;33:94–104. https://doi.org/10.1111/j.1460-2695.2009.01420.x.

[39] Abdalla AO, Amrin A, Muhammad S. Effect of heat treatment parameters on the microstructure and microhardness of Ti-6Al-4V alloy Effect of Heat treatment Parameters on the Microstructure and Microhardness of Ti-6Al-4V Alloy. AIP Conf Proc 2017;1865:030001. https://doi.org/10.1063/1.4993335.

[40] Gupta A, Bennett CJ, Sun W. The role of defects and characterisation of tensile behaviour of EBM additive manufactured Ti-6Al-4V : an experimental study at elevated temperature. Eng Fail Anal 2020:105115. https://doi.org/10.1016/j.engfailanal.2020.105115.

[41] Becker TH, Kumar P, Ramamurty U. Fracture and fatigue in additively manufactured metals. Acta Mater 2021;219:117240. https://doi.org/10.1016/j.actamat.2021.117240.

[42] Luo YR, Huang CX, Tian RH, Wang QY. Effects of strain rate on low cycle fatigue behaviors of high-strength structural steel. J Iron Steel Res Int 2013;20:50–6. https://doi.org/10.1016/S1006-706X(13)60126-0.